

Quarterly Technical Report

Solid State Research

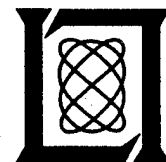
19970128 155

1996:2

Lincoln Laboratory

MASSACHUSETTS INSTITUTE OF TECHNOLOGY

LEXINGTON, MASSACHUSETTS



Prepared for the Department of the Air Force under Contract F19628-95-C-0002.

Approved for public release; distribution is unlimited.

DTIC QUALITY INSPECTED 1

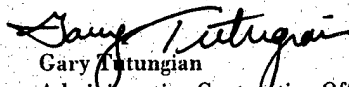
This report is based on studies performed at Lincoln Laboratory, a center for research operated by Massachusetts Institute of Technology. The work was sponsored by the Department of the Air Force under Contract F19628-95-C-0002.

This report may be reproduced to satisfy needs of U.S. Government agencies.

The ESC Public Affairs Office has reviewed this report, and it is releasable to the National Technical Information Service, where it will be available to the general public, including foreign nationals.

This technical report has been reviewed and is approved for publication.

FOR THE COMMANDER


Gary Tutungian
Administrative Contracting Officer
Contracted Support Management

Non-Lincoln Recipients

PLEASE DO NOT RETURN

Permission is given to destroy this document
when it is no longer needed.

MASSACHUSETTS INSTITUTE OF TECHNOLOGY
LINCOLN LABORATORY

SOLID STATE RESEARCH

QUARTERLY TECHNICAL REPORT

1 FEBRUARY-30 APRIL 1996

ISSUED 14 JANUARY 1997

Approved for public release; distribution is unlimited.

LEXINGTON

MASSACHUSETTS

Approved for public release; distribution is unlimited.

ABSTRACT

This report covers in detail the research work of the Solid State Division at Lincoln Laboratory for the period 1 February through 30 April 1996. The topics covered are Quantum Electronics, Electrooptical Materials and Devices, Submicrometer Technology, High Speed Electronics, Microelectronics, Analog Device Technology, and Advanced Silicon Technology. Funding is provided primarily by the Air Force, with additional support provided by the Army, DARPA, Navy, BMDO, NASA, and NIST.

TABLE OF CONTENTS

Abstract	iii
List of Illustrations	vii
Table	ix
Introduction	xi
Reports on Solid State Research	xiii
Organization	xxiii
 1. QUANTUM ELECTRONICS	 1
1.1 High-Power Passively <i>Q</i> -Switched Microlasers	1
 2. ELECTROOPTICAL MATERIALS AND DEVICES	 3
2.1 Analysis of Diode Laser–Microlens Alignment Tolerances	3
2.2 Lattice-Matched GaSb/AlGaAsSb Double-Heterostructure Lasers Grown by Organometallic Vapor-Phase Epitaxy	7
 3. SUBMICROMETER TECHNOLOGY	 13
3.1 Laser-Induced Microchemical Etching of Silicon	13
3.2 Calorimetric Measurements of Optical Materials for 193-nm Lithography	17
 4. HIGH SPEED ELECTRONICS	 21
4.1 Piezoelectrically Driven Sample Injection for Microchip Electrophoresis Applications	21
 5. MICROELECTRONICS	 27
5.1 Doping Profiles of Back-Illuminated CCDs	27
 6. ANALOG DEVICE TECHNOLOGY	 29
6.1 High-Power YBCO Microwave Filter	29
 7. ADVANCED SILICON TECHNOLOGY	 35
7.1 Fully Depleted SOI Technology Development	35

LIST OF ILLUSTRATIONS

Figure No.		Page
1-1	Experimental setup for optical parametric amplification of output of high-power passively Q-switched microchip laser using periodically poled lithium niobate (PPLN).	2
2-1	Geometry for calculation of wavefront deformation introduced by transverse misalignment y of diode laser to microlens, whose flat side is attached to the laser output facet. The phase variation along the plane OP' is obtained by evaluating the optical pathlengths. The laser output radiates from S.	3
2-2	Geometry for calculation of wavefront deformation due to transverse misalignment y in a system in which the convex surface of the microlens directly faces the laser. The phase variation along the plane PQ is obtained by evaluating the optical pathlengths. The laser output radiates from S.	4
2-3	Strehl ratio for 2.0- μ m transverse laser-lens misalignment as a function of numerical aperture, calculated for different lens indices and configurations.	6
2-4	Strehl ratio as function of transverse laser-lens misalignment, calculated for 0.5-numerical-aperture microlenses of different indices and configurations.	6
2-5	Double-crystal x-ray diffraction pattern of $Al_{0.3}Ga_{0.7}As_{0.02}Sb_{0.98}$ on GaSb substrate. The smooth line is a simulation.	8
2-6	Dependence of lattice mismatch of AlGaAsSb layers as function of TBAs/(TBAs + TMSb).	8
2-7	Double-crystal x-ray diffraction pattern of GaSb/ $Al_{0.3}Ga_{0.7}As_{0.02}Sb_{0.98}$ double-heterostructure laser.	9
2-8	Pulsed power vs current for GaSb/ $Al_{0.3}Ga_{0.7}As_{0.02}Sb_{0.98}$ double-heterostructure laser.	10
3-1	Schematic representation of laser direct write etching of silicon in a chlorine ambient. By using high-numerical-aperture optics, the reaction zone can be confined to the necessary micrometer resolutions demanded for micro-electronics processing.	13

LIST OF ILLUSTRATIONS (Continued)

Figure No.		Page
3-2	Graph of linewidth vs power for 4- μm laser beam scanned at 5 cm/s in 500 Torr of nitrogen. Similar results were also found in chlorine, although under high thermal bias conditions, some roughening near the periphery of the etched zone from background etching made interpretation of the linewidth more difficult. Results at two different bias temperatures as well as the theoretical curves from the Green's function model are shown.	14
3-3	Volumetric removal rate and scaled linewidth vs power for a 4- μm laser beam spot size. Rectangles for measuring volumetric removal rates were etched by scanning the laser beam at 5 cm/s in 500 Torr of chlorine at two different bias temperatures. Linewidth results previously presented have been scaled by the factors 16 000 and 12 000 $\mu\text{m}^2/\text{s}$ for the 280 and 70°C bias cases, respectively. The ratio Vol/Res is the volumetric removal rate to resolution ratio where the resolution is two times the melt-zone radii.	15
3-4	Volumetric removal rate vs bias temperature using a 4- μm laser beam spot size and the processing conditions listed in Figure 3-3. Also shown are the experimentally determined linewidths scaled by the factor $10^4 (T_{\text{gas}}/T_o)^{0.8} \mu\text{m}^2/\text{s}$, where it is assumed the bias temperature T_{bias} equals the gas ambient temperature T_{gas} . The parameter T_o is a constant and equal to 300 K.	17
3-5	Schematic diagram of laser calorimetry apparatus. The thermoelectric cooler measures laser power absorbed by the sample. The vacuum chamber is enclosed in an environmental control chamber to minimize thermal noise.	18
4-1	Cross-sectional schematic of typical droplet generator.	21
4-2	Experimental setup using piezoelectric-electrophoretic (PE-EP) injection coupled to epifluorescent laser detection and gel-filled capillaries.	22
4-3	Single-droplet PE-EP injection reproducibility and control. Conditions are 800 fmol/ μL FAM-labeled 18-mer oligonucleotides, $E = 250 \text{ V/cm}$, $L_{\text{eff}} = 25 \text{ cm}$.	23
5-1	Concentration profile of boron dopant on back side of back-illuminated charge-coupled devices.	28

LIST OF ILLUSTRATIONS (Continued)

Figure No.		Page
6-1	Pattern for 9-pole filter. The keyhole-like feature in the center is YBaCuO covered with silver. A similarly shaped spectrum in the package cover makes contact with this pattern using indium washers.	29
6-2	Package and tuning mechanism for a 9-pole filter. The package is made of titanium whose expansion coefficient closely matches that of LaAlO ₃ .	31
6-3	Measured frequency response of 9-pole filter for input power of 7.3 dBm. Shown are the frequencies that were used for high-power CW measurements.	32
6-4	Output power as a function of input power for the eight frequencies indicated in Figure 6-3.	32
6-5	Calculated transient response of 9-pole Chebyshev filter having a 0.6% bandwidth and 1% ripple. The pulse length was 500 ns and the center frequency 2.0 GHz.	33
6-6	Pulsed response for 9-pole filter for different input powers. The RF input pulse was generated by a synthesizer and the transient response measured using a signal analyzer. A number of attenuators were cascaded to prevent saturation of the signal analyzer.	34
7-1	Fully depleted transistor results for 50-nm silicon-on-insulator thickness and $W/L = 7/0.25 \mu\text{m}$: (a) <i>n</i> -channel characteristic curves, (b) <i>p</i> -channel characteristic curves, (c) <i>n</i> -channel subthreshold curves, and (d) <i>p</i> -channel subthreshold curves.	36
7-2	Ring oscillator stage delay vs power supply voltage.	37
7-3	Power delay product of 25-stage, 0.25- μm ring oscillator with fanout of 3.	37

TABLE

Table No.		Page
3-1	Measured Absorption Coefficients at 193 nm for a Variety of Fused Silica and Calcium Fluoride Samples	19

INTRODUCTION

1. QUANTUM ELECTRONICS

When pumped with a 12-W fiber-coupled diode laser, passively *Q*-switched microlasers have produced 157- μ J pulses with 1-ns duration. The 1.064- μ m output has been frequency quadrupled into the ultraviolet with 24% efficiency, and has been used to drive optical parametric oscillators to generate eyesafe radiation at 1.6 μ m.

2. ELECTROOPTICAL MATERIALS AND DEVICES

Aberrations introduced by misalignment between diode lasers and large-numerical-aperture microlenses have been analyzed. A recently advanced packaging technique, in which the precisely polished substrate of a mass-transported microlens is directly attached to the laser, has a major advantage of considerably greater alignment tolerances.

AlGaAsSb epilayers have been grown lattice matched to GaSb substrates using tertiarybutylarsine in organometallic vapor phase epitaxy. Lattice-matched GaSb/AlGaAsSb double-heterostructure lasers have been demonstrated for the first time.

3. SUBMICROMETER TECHNOLOGY

Three-dimensional micromachining techniques, based on laser-induced chemical reactions, have been developed for fabricating microelectromechanical systems. This process offers a new means to optimize the shapes and contours of mechanical components.

A calorimetric technique has been developed for measuring the absorption coefficient of optical materials at 193-nm wavelength. The measurement apparatus has been optimized to be insensitive to fluctuations in the incident illumination and only weakly affected by errors in surface reflectivity.

4. HIGH SPEED ELECTRONICS

A coupled piezoelectric-electrophoretic sample injection technique has been used to achieve accurate volumetric control in the 100-pL range for high-resolution separations. Such improved, automatable means of small-volume sample injection are required for high-density miniaturized instruments for biological and chemical analysis, especially those making use of recent advances in microelectromechanical systems, where sample-loading technology currently limits the effective advantages gained in the areas of channel miniaturization and multiplexing.

5. MICROELECTRONICS

Concentration profiles have been measured for both furnace-annealed and laser-annealed back-illuminated charge-coupled devices. The difference in profiles helps to explain the superior performance of the furnace-annealed devices.

6. ANALOG DEVICE TECHNOLOGY

Measurements have been performed on the rf power dependence, both CW and pulsed, of the frequency response of a 0.6% bandwidth, 9-pole YBaCuO superconductive filter centered at 2 GHz. A CW 1-dB compression level of 6 W has been demonstrated.

7. ADVANCED SILICON TECHNOLOGY

A fully depleted silicon-on-insulator fabrication process with 0.25- μm drawn gate lengths has been developed and is up and running in Lincoln's Microelectronics Laboratory. Ring oscillator delays of 30 ps have been demonstrated, and a radiofrequency amplifier has operated successfully with 1.6-GHz bandwidth.

REPORTS ON SOLID STATE RESEARCH

1 FEBRUARY THROUGH 30 APRIL 1996

PUBLICATIONS

- | | | |
|--|---|--|
| Optically Pumped GaN/Al _{0.1} Ga _{0.9} N
Double-Heterostructure Ultraviolet
Laser | R. L. Aggarwal
P. A. Maki
R. J. Molnar
Z. L. Liao
I. Melngailis | <i>J. Appl. Phys.</i> 79 , 2148
(1996) |
| Frequency and Temperature Dependence
of the Microwave Surface Impedance
of YBa ₂ Cu ₃ O _{7-δ} Thin Films in a DC
Magnetic Field: Investigation
of Vortex Dynamics | N. Belk
D. E. Oates
D. A. Feld
G. Dresselhaus*
M. S. Dresselhaus* | <i>Phys. Rev. B</i> 53 , 3459
(1996) |
| Breakdown of Overlapping-Gate
GaAs MESFET's | C. L. Chen | <i>IEEE Trans. Electron Devices</i>
43 , 535 (1996) |
| Self-Aligned Complementary GaAs
MISFETs Using a Low-Temperature-
Grown GaAs Gate Insulator | C. L. Chen
L. J. Mahoney
K. B. Nichols
E. R. Brown | <i>Electron Lett.</i> 32 , 407
(1996) |
| Mid-Infrared Lasers Fabricated from
III-V Compound Semiconductors | H. K. Choi | <i>Current Opinion Solid State
Mater. Sci.</i> 1 , 212 (1996) |
| 175 K Continuous Wave Operation
of InAsSb/InAlAsSb Quantum-Well
Diode Lasers Emitting at 3.5 μ m | H. K. Choi
G. W. Turner
M. J. Manfra
M. K. Connors | <i>Appl. Phys. Lett.</i> 68 , 2936
(1996) |

*Author not at Lincoln Laboratory.

- | | | |
|---|--|--|
| InAsSb/InAlAsSb Quantum-Well
Diode Lasers Emitting Beyond 3 μm | H. K. Choi
G. W. Turner
M. J. Manfra
M. K. Connors
F. P. Herrmann
A. Baliga*
N. G. Anderson* | <i>Proc. SPIE</i> 2682 , 234
(1996) |
| Nondegenerate Four-Wave Mixing
Wavelength Conversion in Low-Loss
Passive InGaAsP-InP Quantum-Well
Waveguides | J. P. Donnelly
H. Q. Le
E. A. Swanson
S. H. Groves
A. Darwish*
E. P. Ippen* | <i>IEEE Photon. Technol.
Lett.</i> 8 , 623 (1996) |
| Laser Assisted Focused-Ion-Beam-
Induced Deposition of Copper | J. Funatsu*
C. V. Thompson*
J. Melngailis*
J. N. Walpole | <i>J. Vac. Sci. Technol. B</i>
14 , 179 (1996) |
| Comparison of Electric Field Emission
from Nitrogen-Doped, Type Ib
Diamond, and Boron-Doped Diamond | M. W. Geis
J. C. Twichell
N. N. Efremow
K. Krohn
T. M. Lyszczarz | <i>Appl. Phys. Lett.</i> 68 , 2294
(1996) |
| Experimental Study of the Effect of
Quantum-Well Structures on the
Thermoelectric Figure of Merit | L. D. Hicks*
T. C. Harman
X. Sun*
M. S. Dresselhaus* | <i>Phys. Rev. B</i> , 53 , R10 493
(1996) |
| Plasma-Deposited Silylation Resist for
193 nm Lithography | M. W. Horn
M. Rothschild
B. E. Maxwell
R. B. Goodman
R. R. Kunz
L. M. Eriksen | <i>Appl. Phys. Lett.</i> 68 , 179
(1996) |

*Author not at Lincoln Laboratory.

Laser Radar Component Technology	I. Melngailis W. E. Keicher C. Freed S. Marcus B. E. Edwards A. Sanchez T. Y. Fan D. L. Spears	<i>Proc. IEEE</i> 84 , 227 (1996)
193-nm Lithography	M. Rothschild A. R. Forte M. W. Horn R. R. Kunz S. C. Palmateer J. H. C. Sedlacek	<i>Proc. SPIE</i> 2703 , 398 (1996)
Laser Linking of Metal Interconnects: Analysis and Design Considerations	Y. Shen* S. Suresh* J. B. Bernstein	<i>IEEE Trans. Electron Devices</i> 43 , 402 (1996)
Microwave Intermodulation Products and Excess Critical Current in YBa ₂ Cu ₃ O _{7-x} Josephson Junctions	T. C. L. G. Sollner J. P. Sage D. E. Oates	<i>Appl. Phys. Lett.</i> 68 , 1003 (1996)
Analysis of N × M Waveguide Splitters and Couplers with Multimode Guiding Sections	E. R. Thoen* L. A. Molter* J. P. Donnelly	In <i>Guided-Wave Optoelectronics</i> , T. Tamir, ed. (Plenum, New York, 1995), p. 143
Low Oxygen and Carbon Incorporation in AlGaAs Using Tritertiarybutyl- aluminum in Organometallic Vapor Phase Epitaxy	C. A. Wang S. Salim* K. F. Jensen* A. C. Jones*	<i>J. Electron. Mater.</i> 25 , 771 (1996)
Microchip Lasers Create Light in Small Spaces	J. J. Zayhowski	<i>Laser Focus World</i> , 73, April 1996
Ultraviolet Generation with Passively Q-Switched Microchip Lasers	J. J. Zayhowski	<i>Opt. Lett.</i> 21 , 588 (1996)

*Author not at Lincoln Laboratory.

ACCEPTED FOR PUBLICATION

Microwave Analog Optical Links Using Sub-octave Linearized Modulators	G. E. Betts F. J. O'Donnell	<i>IEEE Photon. Technol. Lett.</i>
High Zenithal Directivity from a Dipole Antenna on a Photonic Crystal	E. R. Brown O. B. McMahon	<i>Appl. Phys. Lett.</i>
Diamond Emitters Fabrication and Theory	M. W. Geis J. C. Twichell T. M. Lyszczarz	<i>J. Vac. Sci. Technol. B</i>
High Thermoelectric Figures of Merit in PbTe Quantum Wells	T. C. Harman D. L. Spears M. J. Manfra	<i>J. Electron. Mater.</i>

PRESENTATIONS[†]

Efficient, Single-Mode, 1.5-mJ, Passively <i>Q</i> -Switched Diode- Pumped Nd:YAG Laser	T. Y. Fan J. J. Zaykowski R. Afzal*	Advanced Solid-State Lasers Meeting, San Francisco, California, 31 January–3 February 1996
Electron Emission from Diamond	M. W. Geis J. C. Twichell T. M. Lyszczarz K. E. Krohn N. N. Efremow C. A. Marchi	Technical Seminar, RCA, Princeton, New Jersey, 7 February 1996
A 9-Bit Charge-to-Digital Converter for Integrated Image Sensors	S. A. Paul H-S. Lee*	1996 IEEE International Conference on Solid-State Circuits, San Francisco, California, 7-9 February 1996

*Author not at Lincoln Laboratory.

[†]Titles of presentations are listed for information only. No copies are available for distribution.

Microchip Lasers

J. J. Zayhowski

Lincoln Laboratory
Technical Seminar Series,
Colorado State University,
Fort Collins, Colorado,
27 February 1996

High Power High Brightness
Mid-Infrared Semiconductor Lasers
with Wide Wavelength Tuning Range

H. Q. Le
J. R. Ochoa
G. W. Turner
Y.-H. Zhang*

1996 Pittsburgh Conference,
Chicago, Illinois,
3-8 March 1996

The Linearized Series Mach-Zehnder
Interferometric Modulator for
Sub-octave Analog Links

G. E. Betts
F. J. O'Donnell

Optical Link Using 600 mW
1300 nm Semiconductor Optical
Amplifier as cw Laser Source

G. E. Betts
F. J. O'Donnell
J. P. Donnelly
J. N. Walpole

6th Annual DARPA
Symposium on Photonics
Systems for Antenna
Applications,
Monterey, California,
4-7 March 1996

Protecting Groups for 193-nm
Photoresists

R. D. Allen*
R. Sooriyakumaran*
J. Optiz*
G. M. Wallraff*
G. Breyta*
R. A. DiPietro*
D. C. Hofer*
R. R. Kunz
S. Jayaraman*
R. Shick*
B. Goodall*
U. Okoroanyanwu*
C. G. Willson*

SPIE Symposium on
Microlithography '96,
Santa Clara, California,
10-15 March 1996

Plasma-Deposited Silylation Resist for
193-nm Lithography

M. W. Horn
B. E. Maxwell
R. B. Goodman
R. R. Kunz
L. M. Eriksen

*Author not at Lincoln Laboratory.

Limits to Etch Resistance for 193-nm
Single-Layer Resists

R. R. Kunz
S. C. Palmateer
A. R. Forte
R. D. Allen*
G. M. Wallraff*
R. A. DiPietro*
D. C. Hofer*

Bilayer Resist Approach for 193-nm
Lithography

U. Schaedeli*
E. Tinquely*
C. Mertesdorf*
P. Falcigno*
A. Blakeney*
R. R. Kunz

Chemical Approaches Towards
Materials for 193-nm Lithography

U. Schaedeli*
E. Tinquely*
C. Mertesdorf*
P. Falcigno*
N. Muenzel*
A. Blakeney*
R. R. Kunz

Device Application Issues for High- T_c
Passive Microwave Circuits

W. G. Lyons

Opportunities and Issues for High- T_c
Microwave Devices and Subsystems

W. G. Lyons

Flexible, Sub-half-micron CMOS
Fabrication for Low-Power Circuit
and System Design

P. W. Wyatt
J. A. Burns
C. L. Keast

Passively Q -Switched Microchip Lasers
for Environmental Monitoring

J. J. Zayhowski
B. Johnson

SPIE Symposium on
Microlithography '96,
Santa Clara, California,
10-15 March 1996

American Physical Society
Tutorial Session,
St. Louis, Missouri,
17-22 March 1996

1996 Government Microcircuit
Applications Conference,
Kissimmee, Florida,
18-21 March 1996

Laser Applications to Chemical
and Environmental Analysis
Meeting,
Orlando, Florida,
18-22 March 1996

*Author not at Lincoln Laboratory.

Thermoelectric Properties of
PbEuTe/PbTe Multiple Quantum
Wells

T. C. Harman

15th International Conference
on Thermoelectrics,
Pasadena, California,
26-29 March 1996

Electron Emission from Diamond

M. W. Geis
J. C. Twichell
T. M. Lyszczarz
K. E. Krohn
N. N. Efremow
C. A. Marchi

DARPA Colloquium,
Washington, D. C.,
27 March 1996

High-Performance CCD Imagers
for Low-Light-Level Applications

R. K. Reich

Lincoln Laboratory
Technical Seminar Series,
Colorado State University,
Fort Collins, Colorado,
29 March 1996;
University of Wisconsin,
Madison, Wisconsin,
1 April 1996

Electron Emission from Diamond

M. W. Geis
J. C. Twichell
T. M. Lyszczarz
K. E. Krohn
N. N. Efremow
C. A. Marchi

Ballistic Missile Defense
Organization Technology
Applications Review Meeting,
Boston, Massachusetts,
2-3 April 1996

Nonlinear Microwave Flux Dynamics:
Relationship Between Pinning and
Power Dependence

N. Belk*
D. E. Oates
G. Dresselhaus*
M. S. Dresselhaus*

The Effect of Growth Parameters
on the Quality of Gallium Nitride
Thick Films Grown by Hydride
Vapor Phase Epitaxy

R. J. Molnar
E. Brown

Structural Characterization of High-
Quality GaN Films Grown by Hydride
Vapor Phase Epitaxy

R. Molnar
P. Maki

1996 Spring Meeting of the
Materials Research Society,
San Francisco, California,
8-12 April 1996

*Author not at Lincoln Laboratory.

Gallium Nitride Thick Films Grown
by Hydride Vapor Phase Epitaxy

R. J. Molnar
P. Maki
Z. L. Liao
I. Melngailis

1996 Spring Meeting of the
Materials Research Society,
San Francisco, California,
8-12 April 1996

Progress in Mid-Infrared Diode
Lasers

H. K. Choi
G. W. Turner
C. A. Wang

Solid-State Laser Development at
Lincoln Laboratory

T. Y. Fan
J. J. Zayhowski
T. H. Jeys
V. Daneu
A. Sanchez

9th Annual Diode Laser
Technology Review,
Albuquerque, New Mexico,
15-18 April 1996

Progress on Optically Pumped
Mid-Infrared Semiconductor
Laser Technology

H. Q. Le
G. W. Turner
V. Daneu
J. R. Ochoa
M. J. Manfra
C. Cook

Diamond Cold Cathodes for Flat Panel
Displays

M. W. Geis
J. C. Twichell
T. M. Lyszczarz
K. E. Krohn
N. N. Efremow
C. A. Marchi

1996 ARPA High Definition
Systems Information
Exchange Conference,
Arlington, Virginia,
15-18 April 1996

Progress in Mid-Infrared Diode
Lasers

G. W. Turner
H. K. Choi
M. J. Manfra

Lincoln Laboratory
Technical Seminar Series,
University of Iowa,
Iowa City, Iowa,
19 April 1996

Modulator for Photonic Connectivity

G. E. Betts

IEEE Spring Lecture Series,
Lexington, Massachusetts,
23 April 1996

Electronic Applications of
Superconducting Thin Films

A. A. Anderson

Lincoln Laboratory
Technical Seminar Series,
Massachusetts Institute
of Technology,
Cambridge, Massachusetts,
25 April 1996

Semiconductor Laser Microoptics:
Fabrication, Packaging and Analysis

Z. L. Liao

Technical Seminar,
University of Wisconsin,
Madison, Wisconsin,
25 April 1996

Reflective Linearized Modulator

G. E. Betts
F. J. O'Donnell
K. G. Ray
D. K. Lewis*
D. E. Bossi*
K. Kissa*
G. W. Drake*

Color Separation Echelon Gratings

M. B. Stern
G. J. Swanson

Compact Micro-optical Diode Laser
Assembly Using Mass-Transported
Large-Numerical-Aperture Refractive
Microlenses

D. Z. Tsang
Z. L. Liao
J. N. Walpole

Optical Society of America
Spring Topical Meetings,
Boston, Massachusetts,
28 April–3 May 1996

*Author not at Lincoln Laboratory.

ORGANIZATION

SOLID STATE DIVISION

D. C. Shaver, *Head*
I. Melngailis, *Associate Head*
R. W. Ralston, *Associate Head*
J. F. Goodwin, *Assistant*

A. L. McWhorter, *Fellow*
D. Abusch-Magder, *Research Assistant*
J. T. Chiou, *Research Assistant*
J. P. Mattia, *Research Assistant*
N. L. DeMeo, Jr., *Associate Staff*
J. W. Caunt, *Assistant Staff*
K. J. Challberg, *Administrative Staff*

SUBMICROMETER TECHNOLOGY

M. Rothschild, *Leader*
T. M. Lyszczarz, *Assistant Leader*
L. H. Dubois, *Senior Staff*[†]

Astolfi, D. K.
Bloomstein, T. M.
Craig, D. M.
DiNatale, W. F.
Doran, S. P.
Efremow, N. N., Jr.
Forte, A. R.
Geis, M. W.
Goodman, R. B.
Hartney, M. A.

Horn, M. W.
Kunz, R. R.
Maki, P. A.
Palmacci, S. T.
Palmateer, S. C.
Reinold, J. H., Jr.
Sedlacek, J. H. C.
Stern, M. B.
Twichell, J. C.
Uttaro, R. S.

QUANTUM ELECTRONICS

A. Sanchez-Rubio, *Leader*
T. Y. Fan, *Assistant Leader*

Aggarwal, R. L.
Cook, C. C.
Daneu, V.
DeFeo, W. E.
DiCecca, S.

Dill, C., III
Jeys, T. H.
Le, H. Q.
Ochoa, J. R.
Zayhowski, J. J.

ELECTROOPTICAL MATERIALS AND DEVICES

B. Y. Tsauro, *Leader*
D. L. Spears, *Assistant Leader*
R. C. Williamson, *Senior Staff*

Bailey, R. J.
Betts, G. E.
Chen, C. K.
Choi, H. K.
Connors, M. K.
Donnelly, J. P.
Goodhue, W. D.
Groves, S. H.
Harman, T. C.
Herrmann, F. P.

Hovey, D. L.
Iseler, G. W.
Krohn, L., Jr.
Liau, Z. L.
Manfra, M. J.
McGilvary, W. L.
Missaggia, L. J.
Mull, D. E.
Napoleone, A.
Nee, P.*

Nitishin, P. M.
O'Donnell, F. J.
Paul, S. A.*
Poillucci, R. J.
Reeder, R. E.
Santiago, D. D.
Tsang, D. Z.
Turner, G. W.
Walpole, J. N.
Wang, C. A.

* Research Assistant

[†] Intergovernmental Personnel Act assignment

HIGH SPEED ELECTRONICS

M. A. Hollis, *Leader*
E. R. Brown, *Assistant Leader*[†]
R. A. Murphy, *Senior Staff*

Bozler, C. O.
Calawa, S. D.
Chen, C. L.
Harris, C. T.
Lincoln, G. A., Jr.
Mahoney, L. J.
Mathews, R. H.

McIntosh, K. A.
McMahon, O. B.
Molnar, R. J.
Rabe, S.
Rathman, D. D.
Verghese, S.

ANALOG DEVICE TECHNOLOGY

T. C. L. G. Sollner, *Leader*
L. M. Johnson, *Assistant Leader*
A. C. Anderson, *Senior Staff*

Arsenault, D. R.
Boisvert, R. R.
Brogan, W. T.
Donahue, K. G.
Feld, D. A.
Fitch, G. L.
Gleason, E. F.
Hamm, J. M.
Holtham, J. H.

Lyons, W. G.
Macedo, E. M., Jr.
McClure, D. W.
Murphy, P. G.
Oates, D. E.
Sage, J. P.
Seaver, M. M.
Slattery, R. L.

MICROELECTRONICS

E. D. Savoye, *Leader*
B. B. Kosicki, *Associate Leader*
B. B. Burke, *Senior Staff*

Aull, B. F.
Daniels, P. J.
Doherty, C. L., Jr.
Dolat, V. S.
Donahue, T. C.
Felton, B. J.
Gregory, J. A.
Hotaling, T. C.

Johnson, K. F.
Lind, T. A.
Loomis, A. H.
McGonagle, W. H.
Mountain, R. W.
Percival, K. A.
Reich, R. K.
Young, D. J.

ADVANCED SILICON TECHNOLOGY

C. L. Keast, *Leader*
P. W. Wyatt, *Associate Leader*
A. H. Anderson, *Senior Staff*
J. I. Raffel, *Senior Staff*

Berger, R.
Burns, J. A.
Davis, P. V.
D'Onofrio, R. P.
Frankel, R. S.
Fritze, M.
Herndon, T. O.

Howard, J. F.
Knecht, J. M.
Liu, H. I.
Newcomb, K. L.
Soares, A. M.
Wachtmann, B. K.
Young, G. R.

[†] Intergovernmental Personnel Act assignment

1. QUANTUM ELECTRONICS

1.1 HIGH-POWER PASSIVELY *Q*-SWITCHED MICROLASERS

Two passively *Q*-switched microlasers [1] have been designed and built for use with a 12-W fiber-coupled diode laser pump. The first of these lasers comprises a 3-mm-thick piece of Nd:YAG (1.1% Nd) bonded to a 3-mm-thick piece of Cr⁴⁺:YAG (absorption coefficient of 0.15 mm⁻¹ at 1.064 μ m), with a 40% output coupler. The device is longitudinally pumped, with the output facet of the pump fiber (550- μ m core diameter) imaged in the Nd:YAG with a demagnification of ~ 2 and positioned for minimum threshold. At a pulse repetition rate of 500 Hz, this laser produces 127 μ J in a 500-ps pulse (full width at half-maximum). The output is single frequency and TEM₀₀, with a waist radius of 80 μ m. However, the combination of the high peak intensity of the pulse, the high fluence, and the pump-induced thermal stress in the laser crystals results in damage to both the input and output coatings, extinguishing the laser in a matter of seconds.

The second laser comprises a 3-mm-thick piece of Nd:YAG, a 3-mm-thick piece of Cr⁴⁺:YAG, and a 6-mm-thick piece of Nd:YAG, bonded together in that order, with a 40% output coupler. Pumped in the same manner as the device discussed above, this laser produces 157 μ J in a 0.9-ns pulse. At pulse repetition rates < 2 kHz the output is single frequency and TEM₀₀, with a waist radius of 94 μ m. This device appears to have no lifetime problems at < 2 kHz. At higher repetition rates it becomes increasingly difficult to maintain single-mode performance of the laser.

The high peak intensity of the 0.9-ns laser discussed above makes it ideal for nonlinear optics. By placing a 5-mm-long piece of KTP approximately 1 cm from the output facet of the device we obtain a second-harmonic conversion efficiency of 55%, resulting in 86 μ J/pulse at 532 nm. When this green radiation is imaged 1-to-1 in a 5-mm-long piece of BBO it results in 44% conversion of the green to the UV, generating 38 μ J/pulse at 266 nm. Using a 1-mm-long piece of BBO results in 18 μ J/pulse of UV radiation.

We also transmitted (single pass) the infrared output of this laser through a 15-mm-long piece of periodically poled lithium niobate ($d_{\text{eff}} = 17$ pm/V, effective interaction length of 13 mm) and observed what appeared to be efficient downconversion to 1.6 μ m. The experimental setup is shown in Figure 1-1. In addition to the 1.6- μ m output, we observed red, green, and blue radiation. These observations are consistent with reported observations of parametric oscillators and are indicative of highly efficient optical parametric amplification [2].

J. J. Zayhowski	T. H. Jeys
C. Dill III	C. Cook
J. L. Daneu	

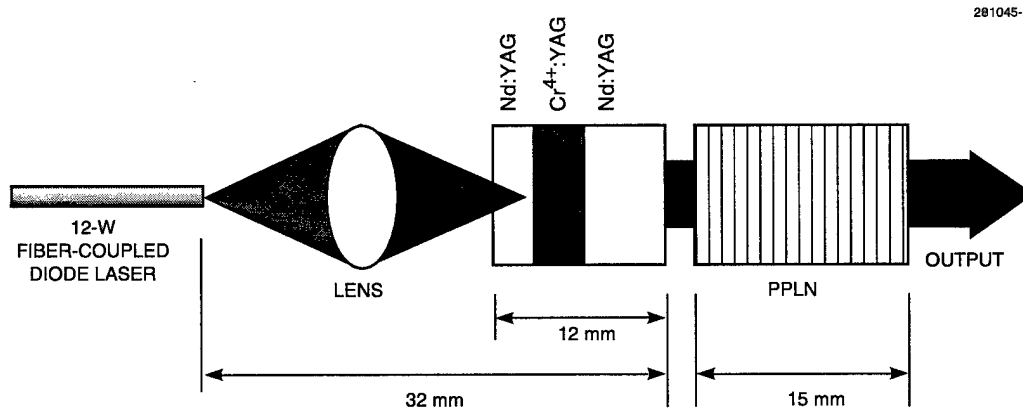


Figure 1-1. Experimental setup for optical parametric amplification of output of high-power passively *Q*-switched microchip laser using periodically poled lithium niobate (PPLN).

REFERENCES

1. J. J. Zayhowski, *Laser Focus World* (Penwell Publishing, Tulsa, Okla., 1996), pp. 73–78.
2. L. E. Myers, R. C. Eckardt, M. M. Feyer, R. L. Byer, W. R. Bosenberg, and J. W. Pierce, *J. Opt. Soc. Am. B* **12**, 2102 (1995).

2. ELECTROOPTICAL MATERIALS AND DEVICES

2.1 ANALYSIS OF DIODE LASER-MICROLENS ALIGNMENT TOLERANCES

Accurate alignment of large-numerical-aperture microlenses, which is required for efficient use of the highly divergent diode laser output, has been a considerable challenge in the development of practical systems [1]–[4]. In this work, we quantitatively analyze the alignment criticalness for different types of microlenses and laser-lens configurations, by evaluating the wavefront deformation introduced by misalignment and calculating the Strehl ratio that characterizes the aberration [5]. In particular, we show that a recently developed packaging technique, in which a mass-transported microlens with precisely polished substrate is directly attached to the laser [4], has a major advantage of considerably greater alignment tolerances.

Two previously used microlens-laser configurations are considered and are illustrated in Figures 2-1 and 2-2, in which the convex surface of the microlens is either on the side toward or away from the laser, respectively. Note that the first configuration is that of the previously described compact packaging technique, in which the microlens substrate is polished to precisely equal the focal length f and then directly attached to the laser heatsink. Here, we consider the tolerance of this configuration for off-axis (or transverse) misalignment, which is represented by the variable y . For illustration of the basic principles, only the simpler cylindrical geometry is considered.

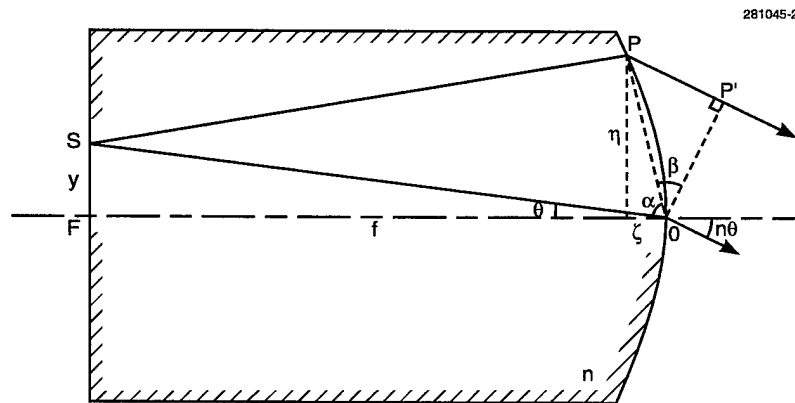


Figure 2-1. Geometry for calculation of wavefront deformation introduced by transverse misalignment y of diode laser to microlens, whose flat side is attached to the laser output facet. The phase variation along the plane OP' is obtained by evaluating the optical pathlengths. The laser output radiates from S.

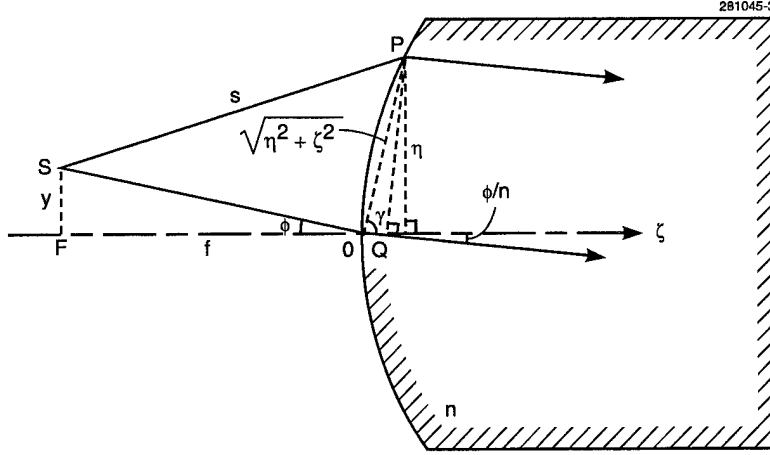


Figure 2-2. Geometry for calculation of wavefront deformation due to transverse misalignment y in a system in which the convex surface of the microlens directly faces the laser. The phase variation along the plane PQ is obtained by evaluating the optical pathlengths. The laser output radiates from S .

Microlenses for exact collimation of a point source are considered, and in the case in Figure 2-1 the lens profile is given by

$$\zeta = \frac{nf}{n+1} \left[1 - \sqrt{1 - \frac{n+1}{n-1} \left(\frac{\eta}{f} \right)^2} \right], \quad (2.1)$$

where ζ is the variation in lens thickness at the coordinate η in the transverse direction, n is the lens refractive index, and $f(\equiv \overline{FO})$ is the focal length. For a small off-axis misalignment $y \ll f$, the output beam is steered by an angle $n\theta$, where $\theta \equiv \tan^{-1}(y/f)$. However, for the large-numerical-aperture lenses of present interest, the phase front in the near field of the steered beam is no longer flat and will lead to a decrease of power in the central lobe in the far field (with a corresponding increase of power in the side lobes). This decreased power is then characterized by the calculated Strehl ratio.

The phase along the line OP' can be calculated from the optical pathlengths

$$\delta = n\overline{SP} + \overline{PP'} - n\overline{SO}. \quad (2.2)$$

By the geometrical relationships, the pathlength difference can be expressed as

$$\delta = n\sqrt{(f-\zeta)^2 + (\eta-y)^2} + \sqrt{\eta^2 + \zeta^2} \sin\beta - n\sqrt{f^2 + y^2}, \quad (2.3)$$

where

$$\alpha \equiv \tan^{-1}(\eta / \varsigma) \quad (2.4)$$

and

$$\beta \equiv \frac{\pi}{2} - \alpha + n\theta . \quad (2.5)$$

With δ evaluated along the line OP', the Strehl ratio SR can be calculated.

$$SR = \frac{1}{A^2} \left| \int_{-A/2}^{A/2} e^{i2\pi\delta/x} ds \right|^2 , \quad (2.6)$$

where ds is the incremental distance along the line OP' and A is the aperture. Note that by this definition the Strehl ratio represents the peak of the far-field intensity from a uniformly illuminated aperture normalized to the case without phase deviations.

In the lens configuration shown in Figure 2-2, the lens profile is now

$$\varsigma = \frac{f}{n+1} \left[-1 + \sqrt{1 + \frac{n+1}{n-1} \left(\frac{\eta}{f} \right)^2} \right] . \quad (2.7)$$

The pathlength deviations can similarly be derived as

$$\delta = \sqrt{(f+\varsigma)^2 + (\eta-y)^2} - \sqrt{f^2 + y^2} - n\sqrt{\eta^2 + \varsigma^2} \cos\left(\gamma + \frac{\phi}{n}\right) , \quad (2.8)$$

where

$$\gamma \equiv \tan^{-1}(\eta / \varsigma) \quad (2.9)$$

and

$$\phi \equiv \tan^{-1}(y/f) . \quad (2.10)$$

With the phase deviation $2\pi\delta/\lambda$ evaluated across the aperture, the Strehl ratio can again be calculated.

Figure 2-3 shows calculated Strehl ratios as functions of the numerical aperture for a given misalignment y of $2.0 \mu\text{m}$. The calculation was carried out for both lens configurations, each with two different refractive indices. Note that for small numerical apertures, the Strehl ratios approach unity and there is no aberration. This agrees with the general notion of beam steering without degradation in the limit of thin lenses and paraxial beams. For larger numerical apertures, however, the $n = 1.5$ case (corresponding to glass or quartz lenses) with the lens facing the laser shows especially rapid beam degradation, much more so than the corresponding $n = 3.1$ case. An index of 3.1 is typical for microlenses formed in semiconductors such as GaP and InP. In sharp contrast, the configuration with the lens facing out shows virtually no beam degradation, even for $n = 1.5$.

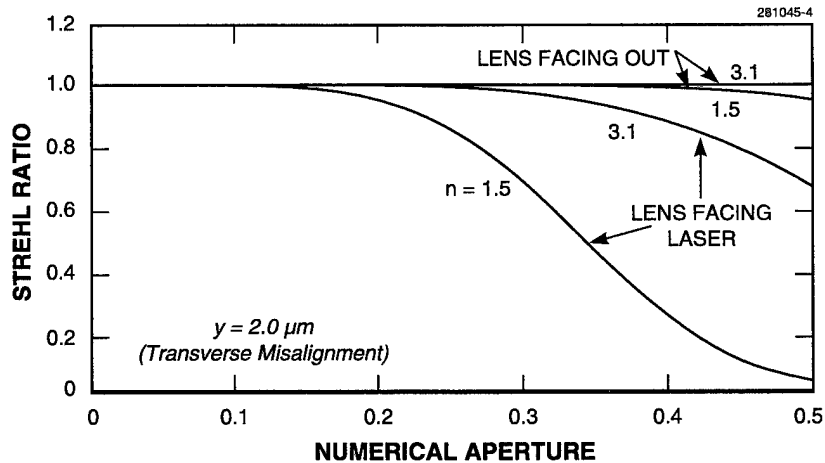


Figure 2-3. Strehl ratio for 2.0- μm transverse laser-lens misalignment as a function of numerical aperture, calculated for different lens indices and configurations.

Figure 2-4 shows calculated Strehl ratios as a function of the misalignment y for a fixed numerical aperture of 0.5. (Note that this large numerical aperture is needed for full collection of the output from most diode lasers.) This plot essentially shows the range of tolerance of the lens alignment. Again, the $n = 1.5$ lens with the convex surface facing the laser needs the most critical alignment, whereas the $n = 3.1$ lens with the convex surface facing out shows virtually no beam degradation for misalignment as large as 5 μm .

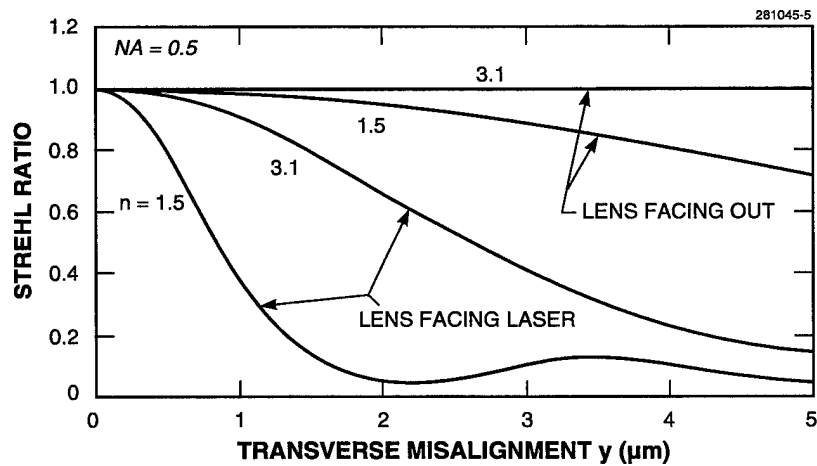


Figure 2-4. Strehl ratio as function of transverse laser-lens misalignment, calculated for 0.5-numerical-aperture microlenses of different indices and configurations.

Thus, for the large numerical apertures needed for efficient collection of the laser output, the alignment tolerance can be very small, e.g., $0.5\ \mu\text{m}$ for maintaining an 80% efficiency, for low-index lenses in an unfavorable configuration. In contrast, with high-index lenses and a more favorable configuration, there is virtually no aberration for misalignment of a few microns. This analysis technique is applicable to other types of errors and provides good guidance for microlens fabrication and system design. The analysis can be straightforwardly extended to circularly symmetric and anamorphic lenses.

Z. L. Liao
J. N. Walpole
D. Z. Tsang

2.2 LATTICE-MATCHED GaSb/AlGaAsSb DOUBLE-HETEROSTRUCTURE LASERS GROWN BY ORGANOMETALLIC VAPOR-PHASE EPITAXY

Previously, we reported low-pressure organometallic vapor-phase epitaxy of n -AlGaSb alloys, and demonstrated room-temperature operation of GaSb/AlGaSb double-heterostructure (DH) diode lasers [6]. The threshold current density was high at $7.5\ \text{kA/cm}^2$ owing to the formation of misfit dislocations in the epilayers, because the AlAsSb is lattice mismatched to the GaSb. All AlGaSb compositions are mismatched with the mismatch reaching 0.65% for AlSb. Here, we report growth of lattice-matched AlGaAsSb on GaSb substrates, and lattice-matched GaSb/AlGaAsSb DH diode lasers with significantly improved performance.

Epitaxial layers were grown on (100) GaSb or semi-insulating GaAs substrates, misoriented 2° toward (110), in a vertical rotating-disk reactor operated at 150 Torr. AlGaAsSb layers were grown at 550°C in a H_2 carrier gas with tritertiarybutylaluminum, triethylgallium, trimethylantimony (TMSb), and tertiarybutylarsine (TBAs). Diethyltellurium diluted in H_2 (50 ppm) and dimethylzinc (1000 ppm in H_2) were used as the n - and p -type doping sources, respectively. Total group III mole fraction was kept constant at 1×10^{-4} , TBAs mole fraction ranged from 8 to 30×10^{-7} , and V/III ratio ranged between 3.0 and 3.6.

The surface morphology of lattice-matched layers, which was examined using Nomarski contrast microscopy, is mirror and featureless, unlike AlGaSb layers that have exhibited a crosshatch pattern [7]. Double-crystal x-ray diffraction (DCXD) was used to measure the lattice mismatch $\Delta a/a$. A scan of a typical $\text{Al}_{0.3}\text{Ga}_{0.7}\text{As}_y\text{Sb}_{1-y}$ layer grown on a GaSb substrate, presented in Figure 2-5, shows Pendellosung fringes, which indicate a uniform layer and a well-defined flat epilayer-substrate interface. The lattice mismatch of -121 arc sec corresponds to $\Delta a/a = 1 \times 10^{-3}$, and x-ray simulation based on the Taupin-Tagachi solution to dynamical x-ray diffraction suggests a $0.45\text{-}\mu\text{m}$ -thick $\text{Al}_{0.3}\text{Ga}_{0.7}\text{As}_{0.02}\text{Sb}_{0.98}$ layer. DCXD scans for $\text{Al}_{0.8}\text{Ga}_{0.2}\text{As}_y\text{Sb}_{1-y}$ layers indicate similar high structural quality. The lattice mismatch of $\text{Al}_{0.3}\text{Ga}_{0.7}\text{As}_y\text{Sb}_{1-y}$ and $\text{Al}_{0.8}\text{Ga}_{0.2}\text{As}_y\text{Sb}_{1-y}$ layers as a function of the ratio of TBAs to the total group-V mole fraction for undoped layers is shown in Figure 2-6. The results indicate excellent controllability of lattice-match conditions with TBAs.

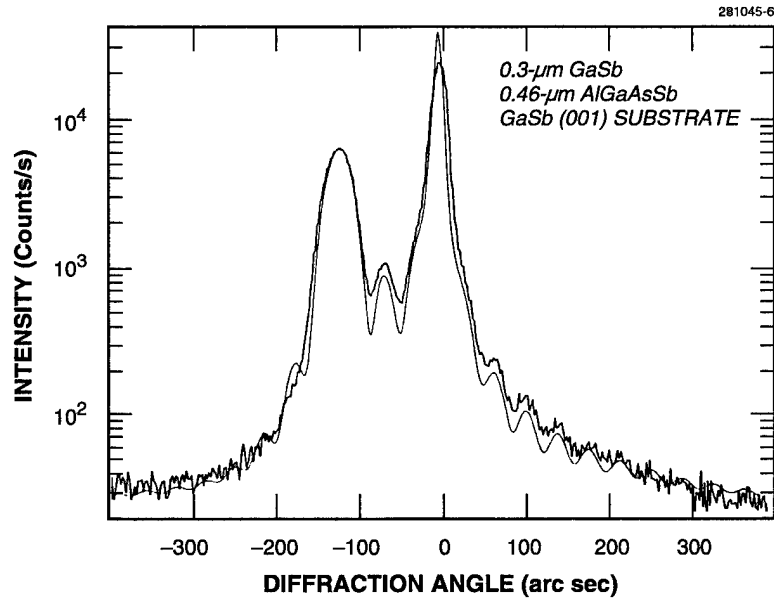


Figure 2-5. Double-crystal x-ray diffraction pattern of $\text{Al}_{0.3}\text{Ga}_{0.7}\text{As}_{0.02}\text{Sb}_{0.98}$ on GaSb substrate. The smooth line is a simulation.

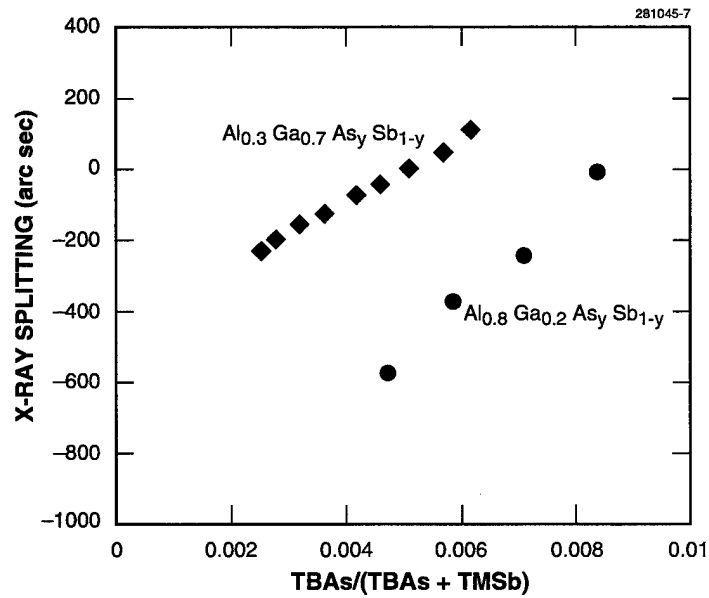


Figure 2-6. Dependence of lattice mismatch of AlGaAsSb layers as function of $\text{TBAs}/(\text{TBAs} + \text{TMSb})$.

Lattice-matched $\text{Al}_x\text{Ga}_{1-x}\text{As}_y\text{Sb}_{1-y}$ layers ($x = 0.3$ and 0.8) are p -type with carrier concentrations within 10 to 20% of the values measured for $\text{Al}_x\text{Ga}_{1-x}\text{Sb}$. To quantify the effect of TBAs on C incorporation, an $\text{Al}_{0.8}\text{Ga}_{0.2}\text{Sb}/\text{Al}_{0.8}\text{Ga}_{0.2}\text{As}_{0.06}\text{Sb}_{0.94}/\text{GaSb}$ multilayer structure was grown for analysis by secondary ion mass spectroscopy. The C level is $4.2 \times 10^{18} \text{ cm}^{-3}$ for the lattice-mismatched layer vs $3.4 \times 10^{18} \text{ cm}^{-3}$ for the lattice-matched layer. These results indicate that C levels are not significantly reduced by the addition of TBAs during growth. The electron concentration of AlGaAsSb layers grown on semi-insulating GaAs substrates as measured from Hall samples is similar to lattice-mismatched layers because the C levels are similar.

A lattice-matched $\text{GaSb}/\text{Al}_{0.3}\text{Ga}_{0.7}\text{As}_{0.02}\text{Sb}_{0.98}$ DH diode laser, which consists of $2.5\text{-}\mu\text{m}$ -thick $n\text{-Al}_{0.3}\text{Ga}_{0.7}\text{As}_{0.02}\text{Sb}_{0.98}$ cladding layer ($\sim 2 \times 10^{17} \text{ cm}^{-3}$), $0.3\text{-}\mu\text{m}$ -thick undoped GaSb active layer, $2\text{-}\mu\text{m}$ -thick $p\text{-Al}_{0.3}\text{Ga}_{0.7}\text{As}_{0.02}\text{Sb}_{0.98}$ cladding layer, and $0.1\text{-}\mu\text{m}$ -thick $p^+\text{-GaSb}$ cap layer, was grown on an $n\text{-GaSb}$ substrate. The p cladding layer was nominally undoped with a hole concentration of $\sim 2 \times 10^{17} \text{ cm}^{-3}$. The value of $\Delta a/a$ determined by DCXD, shown in Figure 2-7, is less than 5×10^{-4} . Broad-area lasers $100 \mu\text{m}$ wide were fabricated in the conventional manner [8], and 500- and $1000\text{-}\mu\text{m}$ -long devices were tested at room temperature with 400-ns pulses at a repetition rate of 1 kHz. The output power vs current is shown in Figure 2-8. The lasers operated at a wavelength of $1.75 \mu\text{m}$ with pulsed threshold current densities of 2.1 and 2.8 kA/cm^2 for 1000- and $500\text{-}\mu\text{m}$ -long devices, respectively. These values are greatly improved over our previous result of 7.5 kA/cm^2 for a $500\text{-}\mu\text{m}$ -long lattice-mismatched DH

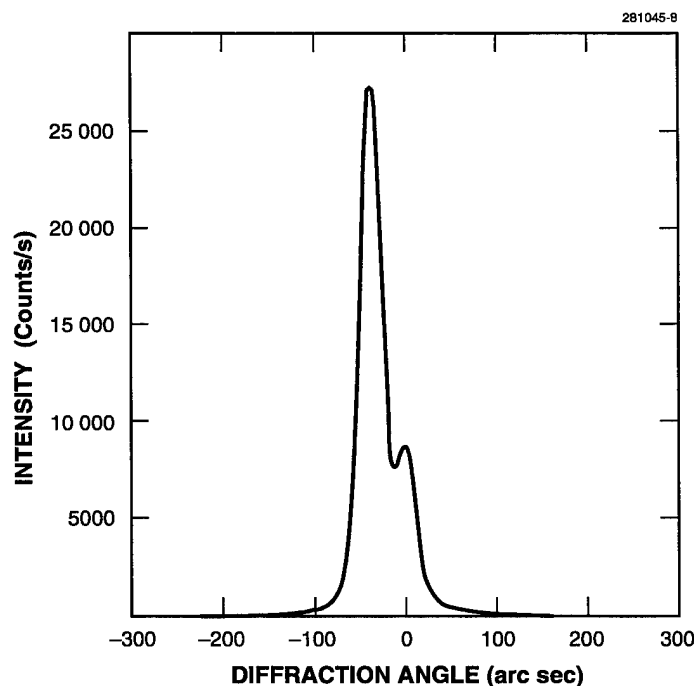


Figure 2-7. Double-crystal x-ray diffraction pattern of $\text{GaSb}/\text{Al}_{0.3}\text{Ga}_{0.7}\text{As}_{0.02}\text{Sb}_{0.98}$ double-heterostructure laser.

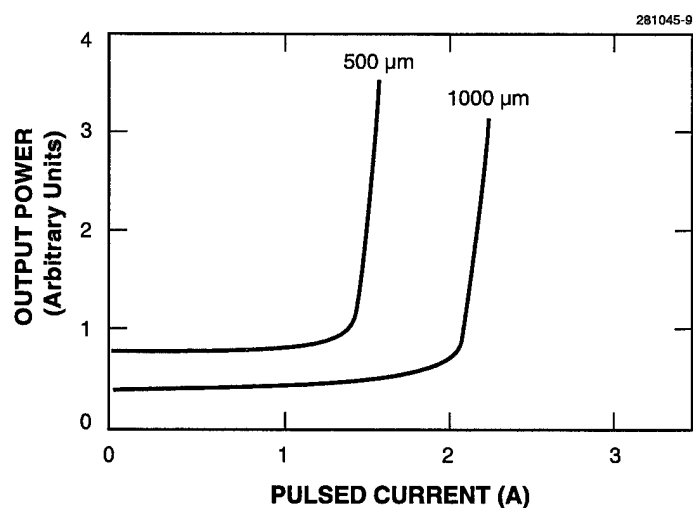


Figure 2-8. Pulsed power vs current for $\text{GaSb}/\text{Al}_{0.3}\text{Ga}_{0.7}\text{As}_{0.02}\text{Sb}_{0.98}$ double-heterostructure laser.

laser [6], and are comparable to values (1.6 kA/cm^2) obtained for devices with similar structures grown by liquid phase epitaxy [9]. $\text{GaInAsSb}/\text{Al}_{0.75}\text{Ga}_{0.25}\text{As}_{0.6}\text{Sb}_{0.94}$ DH lasers grown by molecular beam epitaxy have a threshold current density of 0.94 kA/cm^2 emitting at $2.2 \mu\text{m}$ [10]. Further improvements in device performance are anticipated for structures with higher optical confinement and quantum-well active layers. In addition, reduction in O levels through the use of improved antimony sources will further improve device performance.

C. A. Wang	H. K. Choi
D. R. Calawa	J. W. Chludzinski
W. L. McGilvary	

REFERENCES

1. S. W. Connely and J. J. Snyder, *Proc. SPIE* **2383**, 252 (1995).
2. J. Levy, *Proc. SPIE* **2383**, 278 (1995).
3. R. J. Beach, M. A. Emanuel, B. L. Freitas, J. A. Skidmore, N. W. Carlson, W. J. Benett, and R. W. Solarz, *Proc. SPIE* **2383**, 283 (1995).
4. Solid State Research Report, Lincoln Laboratory, MIT, 1995:3, p. 1.
5. Solid State Research Report, Lincoln Laboratory, MIT, 1995:4, p. 1.
6. C. A. Wang, K. F. Jensen, A. C. Jones, and H. K. Choi, *Appl. Phys. Lett.* **68**, 400 (1996).
7. C. A. Wang, M. C. Finn, S. Salim, K. F. Jensen, and A. C. Jones, *Appl. Phys. Lett.* **67**, 1384 (1995).
8. H. K. Choi and S. J. Eglash, *Appl. Phys. Lett.* **61**, 1154 (1992).
9. A. E. Drakin, P. G. Eliseev, B. N. Sverdlov, A. E. Bochkarev, L. M. Dolginov, and L. V. Druzhinina, *IEEE J. Quantum Electron.* **QE-23**, 1089 (1987).
10. H. K. Choi and S. J. Eglash, *Appl. Phys. Lett.* **59**, 1165 (1991).

3. SUBMICROMETER TECHNOLOGY

3.1 LASER-INDUCED MICROCHEMICAL ETCHING OF SILICON

The emerging field of microelectromechanical systems merges electronics with integrated mechanical components to produce sensors and actuators such as pressure transducers, accelerometers, valves, and pumps [1]. Current techniques for fabricating these mechanical components rely on lithographic techniques that limit shapes to extrusions of two-dimensional patterns. Laser processing offers a new means to optimize the shapes and contours of mechanical components or interconnects, which are inherently more three-dimensional than electronic devices.

The development of a three-dimensional machining technology capable of achieving micrometer-scale resolutions is based on a laser-induced microreaction initially developed for trimming and trench etching in semiconductor processing [2]–[4]. As shown schematically in Figure 3-1, an argon-ion laser is used to locally heat a portion of the silicon substrate in a chlorine ambient. At the onset of melting, volatile silicon chlorides are formed limiting the redeposition of products. Chemical activation also reduces the energy requirement for removal. This minimizes the damage potential relative to other patterning technologies such as laser ablation, electro-discharge machining, or diamond turning, which rely purely on thermal or mechanical energy.

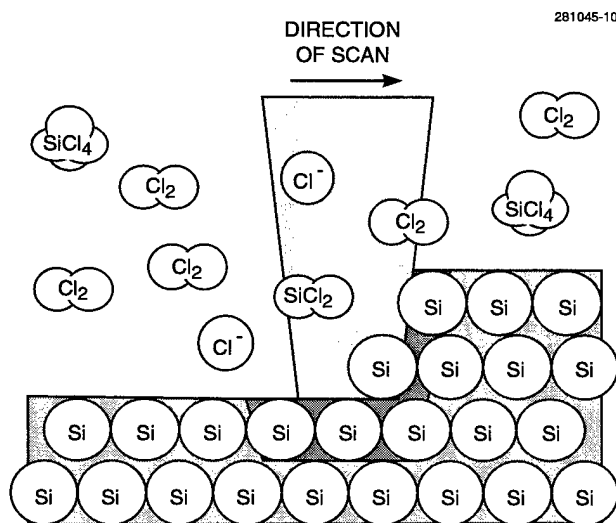


Figure 3-1. Schematic representation of laser direct write etching of silicon in a chlorine ambient. By using high-numerical-aperture optics, the reaction zone can be confined to the necessary micrometer resolutions demanded for microelectronics processing.

A galvanometer-based scanning system was developed to characterize the machining process as the laser power, chlorine pressure, and bias temperature of the substrate were varied [5],[6]. To measure the effective reaction zone size, the laser was rastered for one pass in a serpentine pattern over the surface in an inert atmosphere. The limits of the molten zone are clearly evident by morphological changes on the surface under Nomarski optical imagery. Figure 3-2 shows linewidth data as the laser power is varied using a 4- μm laser spot size and 5-cm/s scanning velocity. Also shown are curves for the predicted values using a simple model based on Green's function techniques [7]. The model is similar to that presented by Cohen et al. [8] in their studies of laser-induced diode linking but solves directly for the steady-state melt-zone radius without their more general, but computationally more intense, time-stepping approach that requires both spatial and time discretization. The model appears to be in close agreement with the experimental results, confirming the melt-induced nature of the reaction. The deviation near melting was also observed by Tang and Herman [9] in their Raman microprobe studies of silicon at the onset of melting and is believed to be due to convective cooling at the surface, which is not accounted for in the simple model.

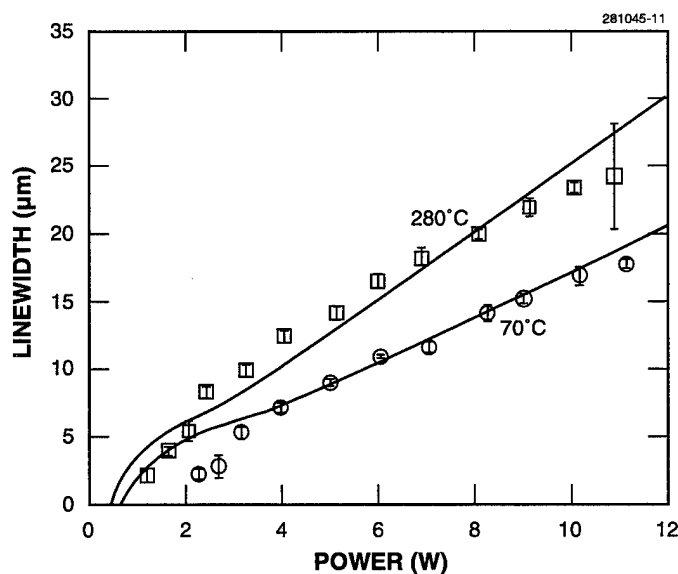


Figure 3-2. Graph of linewidth vs power for 4- μm laser beam scanned at 5 cm/s in 500 Torr of nitrogen. Similar results were also found in chlorine, although under high thermal bias conditions, some roughening near the periphery of the etched zone from background etching made interpretation of the linewidth more difficult. Results at two different bias temperatures as well as the theoretical curves from the Green's function model are shown.

In Figure 3-3, volumetric removal rate measurements from etched rectangles are shown. The operating pressures are sufficiently high that the removal rate has saturated from diffusion limitations. Also shown are the previously obtained linewidth measurements scaled by a constant proportionality factor. The removal rate is found to scale directly with the radius of the molten zone, which is characteristic of systems with three-dimensional transport [10]. This can be shown simply by considering the diffusional flux to a hemispheric-shaped particle sink. The diffusional flux density \bar{J} has the form

$$\bar{J} = -D\nabla c, \quad (3.1)$$

where D is the gas diffusivity and c is the concentration of chlorine. To first order, the flux density at the surface can be estimated from the gradient and is

$$\bar{J} \sim -Dc_{\infty} / x_m. \quad (3.2)$$

In Equation (3.2), c_{∞} is the concentration of the chlorine in the ambient. The characteristic length scale is determined by the geometry of the system and can be estimated to be on the order of the radius of the reaction zone x_m . The total flux is the surface flux density times the area of the melt zone resulting in the linear dependency between removal rate and melt-zone radius. A more careful analysis that considers conductive heating into the gas phase from the molten zone, temperature-dependent gas properties, and

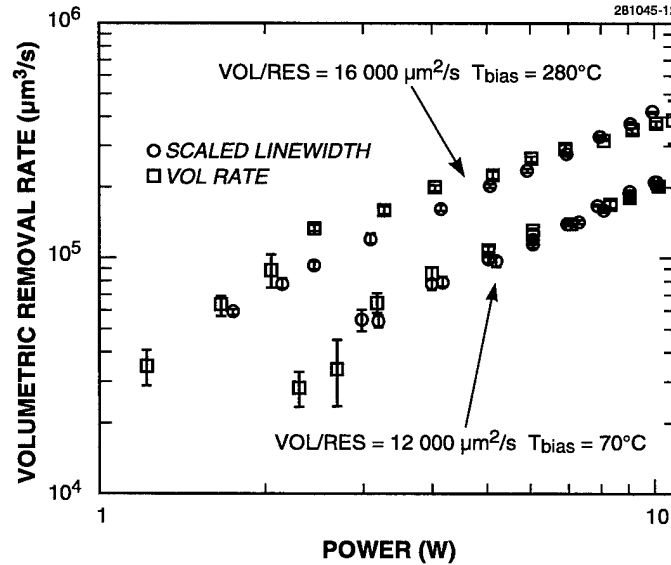


Figure 3-3. Volumetric removal rate and scaled linewidth vs power for a 4-μm laser beam spot size. Rectangles for measuring volumetric removal rates were etched by scanning the laser beam at 5 cm/s in 500 Torr of chlorine at two different bias temperatures. Linewidth results previously presented have been scaled by the factors 16 000 and 12 000 μm²/s for the 280 and 70°C bias cases, respectively. The ratio Vol/Res is the volumetric removal rate to resolution ratio where the resolution is two times the melt-zone radii.

disk-shaped geometry has been performed [7]. The resulting total removal rate is

$$\text{Vol Rate} = 4x_m c D (T_{\text{avg}}) / d_{\text{Si}} , \quad (3.3)$$

where the concentration diffusivity product is evaluated at the average temperature between the melt zone and gas ambient, and the density of silicon d_{Si} is used to convert chlorine flux to silicon removal rate. In the present system, the gas ambient a few boundary layers from the surface is expected to be in thermal equilibrium with the bias temperature of the substrate since the vapor cell coverglass is several millimeters away. Since the melting temperature of silicon ($T_m = 1685$ K) is significantly higher than the range of bias temperatures investigated, the overall removal rate increase is not expected to improve dramatically as the bias temperature is varied, counter to the results from additional tests. This suggests that effects removed from the surface limit transport rates.

The simple model previously summarized has not, however, considered the significant effects gas-phase chemistry can have on the transport rates through heats of reaction and compositional changes. It is believed that the high temperatures surrounding the molten zone allow otherwise highly unstable reaction intermediaries formed at the surface to remain in their dissociated state. As the intermediaries diffuse outwards from the molten surface, they consume inwards diffusing chlorine molecules forming stable SiCl_4 . The extent of this reaction, however, is limited by the relatively high degree of heat released. Through a simple order-of-magnitude estimate, it can be shown that even if a fraction of surface products react within close proximity to the molten zone, the temperature rise can well exceed the melting temperature of silicon [7]. From thermodynamic considerations, SiCl_2 is predicted to be the predominant silicon-chloride at temperatures just below the melting point of silicon. Although thermodynamic equilibrium cannot be assumed, it indicates the driving force of the reaction. The intermediaries will continue to diffuse outwards a greater distance where heats of reaction are spread over a greater volume limiting the temperature rise. Because of the highly reactive nature of the intermediaries, the thermal energy in the cool ambient is sufficient to overcome the energy barrier, allowing the chemistry to proceed rapidly. Numerical techniques are required to fully understand the balance between outdiffusion of SiCl_4 into the ambient, consumption of inwards diffusing Cl_2 by reaction intermediaries, and gas-phase chemical reaction rates in their influence on the overall removal rate, and efforts are currently under way to develop such techniques. However, qualitatively, one would expect a similar scaling behavior as predicted before. The removal rate is expected to be proportional to a characteristic length scale defined by the radius of the melt zone, although in this instance it is more directly related to the spatial extent of the gas-phase chemistry. The concentration diffusivity product, however, is determined by the gas-ambient temperature $T_{\text{gas}}^{0.8}$ rather than the temperature of the molten zone. Since this product is to first order proportional to $T^{0.8}$ for the chlorine system [11], the expected removal rate should be proportional to

$$\text{Vol Rate} \propto x_m T_{\text{gas}}^{0.8} . \quad (3.4)$$

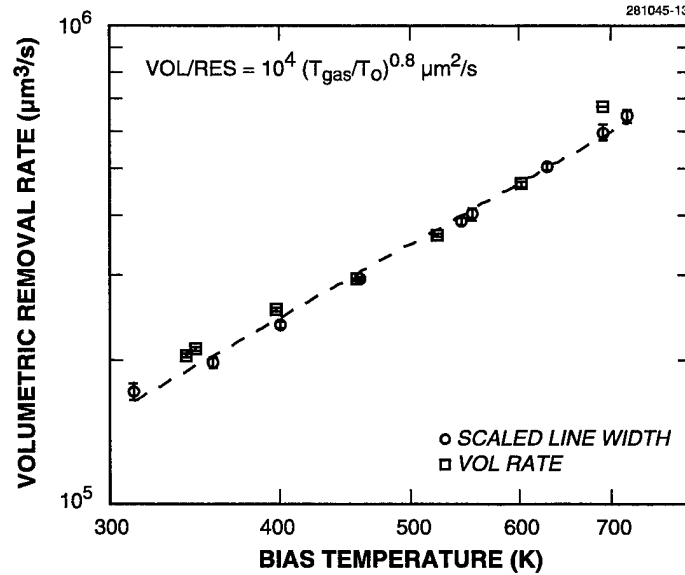


Figure 3-4. Volumetric removal rate vs bias temperature using a 4- μm laser beam spot size and the processing conditions listed in Figure 3-3. Also shown are the experimentally determined linewidths scaled by the factor $10^4 (T_{\text{gas}}/T_o)^{0.8} \mu\text{m}^2/\text{s}$, where it is assumed the bias temperature T_{bias} equals the gas ambient temperature T_{gas} . The parameter T_o is a constant and equal to 300 K.

Shown in Figure 3-4 are the experimental results using the new scaling behavior predicted in Equation (3.4). The results of this model indicate that increasing the bias temperature of the substrate provides a relatively inexpensive means to increase removal rates.

T. M. Bloomstein
S. Palmacci
K. F. Jensen*

3.2 CALORIMETRIC MEASUREMENTS OF OPTICAL MATERIALS FOR 193-nm LITHOGRAPHY

Lithography using a 193-nm ArF excimer laser source is a strong contender to meet the patterning requirements for the 0.18- μm generation and beyond [12]. The most critical issue in the development of 193-nm exposure tools suitable for production is the availability of optical materials that meet stringent specifications for refractive index homogeneity, surface finish, and absorbance. While techniques already exist for measuring all three properties, it has been apparent that a new approach was required to quantify

*Author not at Lincoln Laboratory.

absorption with accuracy significantly better than the target specification of 0.001 cm^{-1} . Calorimetry has been shown to be an effective approach for measuring absorption [13]. Here, we describe the development of optimized apparatus and techniques for implementing this approach.

Radiation absorbed in a sample that is neither scattered nor reemitted as fluorescence generates phonons, hence heat. Thus, the absorption coefficient can be determined by measuring this heat as well as the flux of the beam leaving the sample. Since the uncertainty of the result is approximately the sum of the percentage uncertainties of these measurements, the outcome is substantially independent of illumination fluctuations, which is an important consideration when using an excimer laser source. Also, the result is only weakly dependent on errors in surface reflectivity. The central challenge is to accurately measure absorbed heat.

The apparatus illustrated in Figure 3-5 was constructed to accurately measure the absorbed heat using a thermoelectric cooler (TEC). The sample is thermally matched to a copper plate bonded to the TEC, and a large copper heat sink underneath the TEC serves as a thermal reservoir. Each of the three interfaces was bonded with a thermally conductive compound consisting of Krytox oil and zinc oxide. The relatively uniform central portion of the 193-nm laser beam was extracted by a rectangular aperture ($5 \times 10 \text{ mm}^2$), directed through the sample, and passed out the far side where it was collected by a power meter. The assembly was housed in a vacuum chamber which in turn was enclosed in a temperature-stabilized environment ($\pm 0.05^\circ\text{C}$). The system operates in a nitrogen ambient of $\sim 1 \text{ Torr}$ to reduce convective losses.

The TEC is an array of semiconductor P-N junctions with two key properties. First, when a current I is injected, heat proportional to I is pumped from one side to the other (the Peltier effect). Second, accounting for resistive loss, the voltage across the device is proportional to the differential temperature

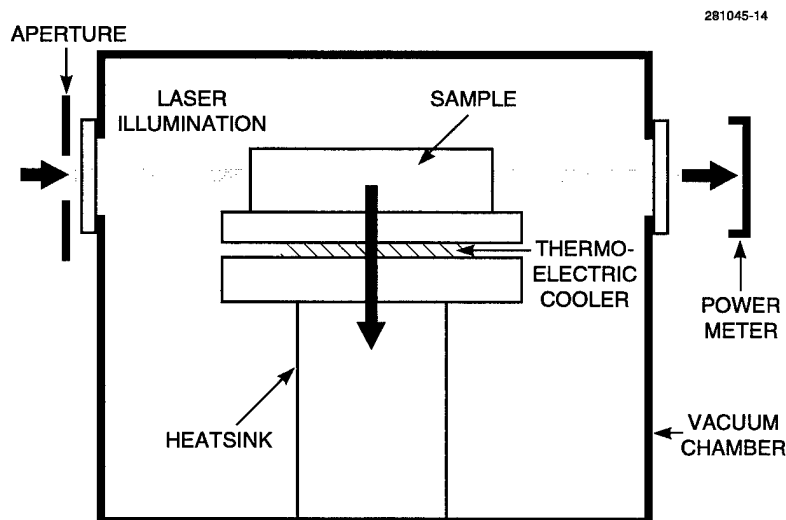


Figure 3-5. Schematic diagram of laser calorimetry apparatus. The thermoelectric cooler measures laser power absorbed by the sample. The vacuum chamber is enclosed in an environmental control chamber to minimize thermal noise.

ΔT between its two layers (the Seebeck effect). Combining the Peltier effect with conduction, the heat flow across the TEC is

$$Q = (2N\alpha T_c)I + (2NkG)\Delta T, \quad (3.5)$$

where N is the number of junctions, α is the Seebeck coefficient, T_c is the mean operating temperature of the TEC, k is the thermal conductivity, and G is a geometry factor (TEC effective area/thickness). The corresponding voltage is

$$V = (2N\rho/G)I - (2N\alpha)\Delta T. \quad (3.6)$$

A bismuth telluride TEC was selected with $N = 63$, $k = 1.5 \times 10^{-2}$ W/cm K at $T_c = 296$ K, and a surface area of 15×30 mm² with $G = 0.064$ cm. Through calibration, we found $\alpha = 2.041 \times 10^{-4}$ V/K and $\rho = 1.14 \times 10^{-3}$ Ω cm.

The absorption measurements were made by driving current through the TEC until the voltage across it indicated a zero temperature differential ($\Delta T = 0$). No heat is conducted across the TEC, so heat flow is proportional to the current required to sustain this isothermal equilibrium. This approach minimizes radiative transfer to the chamber walls by pumping the absorbed heat away from the sample. The apparatus shown in Figure 3-5 was able to track differential temperature to better than 0.001 K and measure absorbed power to within 0.1 mW (1 σ), which provides sufficient sensitivity to make measurements at fluences in the vicinity of 10 mJ/cm². This fluence corresponds to an incident power of 1 W, which in a 4-cm sample at the target absorption of 0.001 cm⁻¹ yields an absorbed power of ~ 10 mW, resulting in an excellent signal-to-noise ratio (100:1).

Absorption measurements were made for a variety of samples of different grades from several suppliers. All samples had the dimensions $10 \times 20 \times 40$ mm³ and were finished by the same polisher. The results are summarized in Table 3-1.

TABLE 3-1
Measured Absorption Coefficients at 193 nm for a Variety of Fused Silica and Calcium Fluoride Samples

Material	Number of Samples	Absorption β (cm ⁻¹)	
		Mean	Range
Fused silica A	6	0.0033	0.0012
Fused silica B	2	0.0037	0.0005
Fused silica C	6	0.011	0.013
Fused silica D	7	0.0038	0.0007
Fused silica E	1	0.0038	—
Calcium fluoride	2	0.0018	0.0001

There is significant variation in absorption not only between material grades from different vendors, but also within material from the same batch. This may be due to measurement error or sample inhomogeneities. Repeated measurements from the same sample show better than 10% reproducibility in the absence of the extra absorption described above, so it is likely that most of the variation is indeed present in the material, at least for samples A and C. None of the samples approaches the target absorption of 0.001 cm^{-1} . Observing the fluorescence of the sample indicates that the surfaces contribute more strongly to the absorption than does the volume, and consequently these measurements may be limited primarily by surface absorption. A more thorough investigation of this is under way using absorption coefficients from more than one pathlength.

A. Grenville	M. Rothschild
R. Uttaro	J. H. C. Sedlacek
D. Corliss	

REFERENCES

1. K. E. Petersen, *Proc. IEEE* **70**, 420 (1982).
2. D. J. Ehrlich, R. M. Osgood, Jr., and T. F. Deutsch, *Appl. Phys. Lett.* **38**, 1018 (1981).
3. G. V. Treyz, R. Beach, and R. M. Osgood, Jr., *J. Vac. Sci. Technol. B* **6**, 37 (1988).
4. G. V. Treyz, R. Beach, and R. M. Osgood, Jr., *Appl. Phys. Lett.* **50**, 475 (1987).
5. T. M. Bloomstein and D. J. Ehrlich, *Appl. Phys. Lett.* **61**, 708 (1992).
6. T. M. Bloomstein and D. J. Ehrlich, *Technical Digest of Transducers '91* (IEEE, New York, 1992), p. 507.
7. T. M. Bloomstein, Sc.D. thesis, Massachusetts Institute of Technology, 1996.
8. S. S. Cohen, P. W. Wyatt, G. H. Chapman, and J. M. Canter, *IEEE Trans. Electron Devices* **35**, 1533 (1988).
9. H. Tang and I. P. Herman, *J. Appl. Phys.* **71**, 3492 (1992).
10. D. J. Ehrlich and J. Y. Tsao, *J. Vac. Sci. Technol. B* **1**, 969 (1983).
11. R. B. Bird, W. E. Stewart, and E. N. Lightfoot, *Transport Phenomena* (John Wiley, New York, 1960), p. 78.
12. M. Rothschild, A. R. Forte, M. W. Horn, S. C. Palmateer, and J. H. C. Sedlacek, *IEEE J. Select. Topics Quantum Electron.* **1**, 916 (1995).
13. Solid State Research Report, Lincoln Laboratory, MIT, 1995:2, p. 3.

4. HIGH SPEED ELECTRONICS

4.1 PIEZOELECTRICALLY DRIVEN SAMPLE INJECTION FOR MICROCHIP ELECTROPHORESIS APPLICATIONS

High-density miniaturized instruments for biological and chemical analysis will require improved, automatable means of small-volume sample injection. This is especially true of instruments making use of recent advances in microelectromechanical systems, where sample-loading technology currently limits the effective advantages gained in the areas of channel miniaturization and multiplexing. We have demonstrated the use of a coupled piezoelectric-electrophoretic (PE-EP) sample injection technique to achieve accurate volumetric control and high resolution. The PE-EP injection scheme consists of a two-step process: piezoelectrically driven droplet injection of the sample to the entrance of the separation channel, and rapid electrophoresis into the separation channel to prevent lateral diffusion and convection effects. There are many advantages intrinsic to the PE-EP injection method: minimal volumes of sample are required, volumetric control of injected sample can be controlled in a quantized fashion, and the reduction of sample plug length to the diffusion-limited regime allows maximum throughput at high resolution.

We are using prototype droplet generators (MicroFab Technologies), which have a schematic cross section as shown in Figure 4-1. An axisymmetric capillary is surrounded by an annular piezoceramic. The output end of the capillary is tapered to a nozzle, typically on the order of $\sim 60\text{ }\mu\text{m}$. A voltage pulse ($\sim 100\text{ V}$, $30\text{ }\mu\text{s}$) from our custom drive electronics is applied to the piezoelectric ceramic. This causes compression of the glass capillary and creates corresponding acoustic waves in the fluid held within [1]. By performing the proper acoustic tuning of the device, the droplet generator can be designed to eject single 100-pL droplets from the exit orifice. Such droplet generators have been shown to effectively dispense biological materials [2] and have been used in samplers of analytical flow [3]. In our PE-EP method, these droplets are subsequently injected into the separation channel and determine sample plug size.

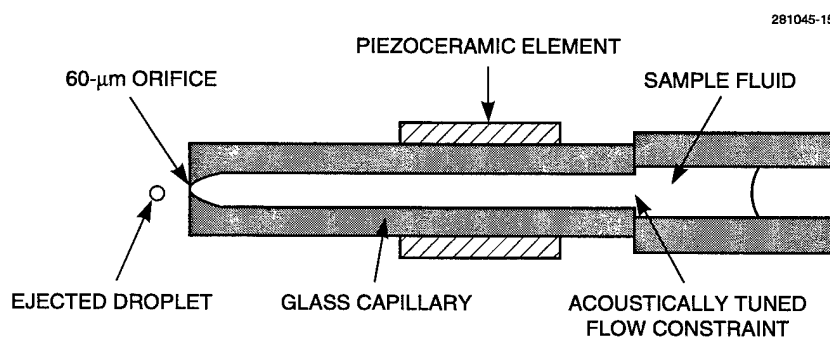


Figure 4-1. Cross-sectional schematic of typical droplet generator.

In Figure 4-2 we show our experimental test arrangement, which we have designed to be used with gel-filled capillaries. Light from a 300-mW multimode argon-ion laser source (1) is passed through a notch filter (2) to select either the 488- or 514-nm line. The beam passes through a beam-splitting/steering device (3a,3b) for injection into an epifluorescent microscope. A portion of the beam is also sent through a mirror combination (4,12) and through a 250-mm focal length lens (13) to illuminate the injection area. Injected fluorescent plugs can be observed directly with a conventional stereoscope (20). The light launched into the microscope column is reflected off a high-reflectance mirror (5), off a beam splitter (6), and through a microscope objective (7), where it is focused on a region of a gel-filled capillary where the polyimide cladding has been removed (8). Fluorescent light is collected through the objective in an epifluorescent mode, through an emission filter (9) to remove unwanted signal, and through a pinhole aperture (10) to achieve limited spatial filtering. The signal then impinges on a photomultiplier tube (11) and is displayed on an x-y plotter. A micropositionable (15) piezoelectrically driven droplet generator (14) is aligned to the input end of the gel-filled capillary. This capillary has been mounted on a plexiglas holder (16) with the plastic removed from the detection area to reduce background fluorescent noise. The buffer reservoir at the output end (19) is a conventional microcentrifuge tube with tris-borate solution and urea as a denaturant. At the input end the buffer reservoir is a well that is machined into the plexiglas (17) and designed to be accessible to the droplet generator. Electrophoretic contacts (18a,18b) to the buffer solutions are made through two platinum electrodes.

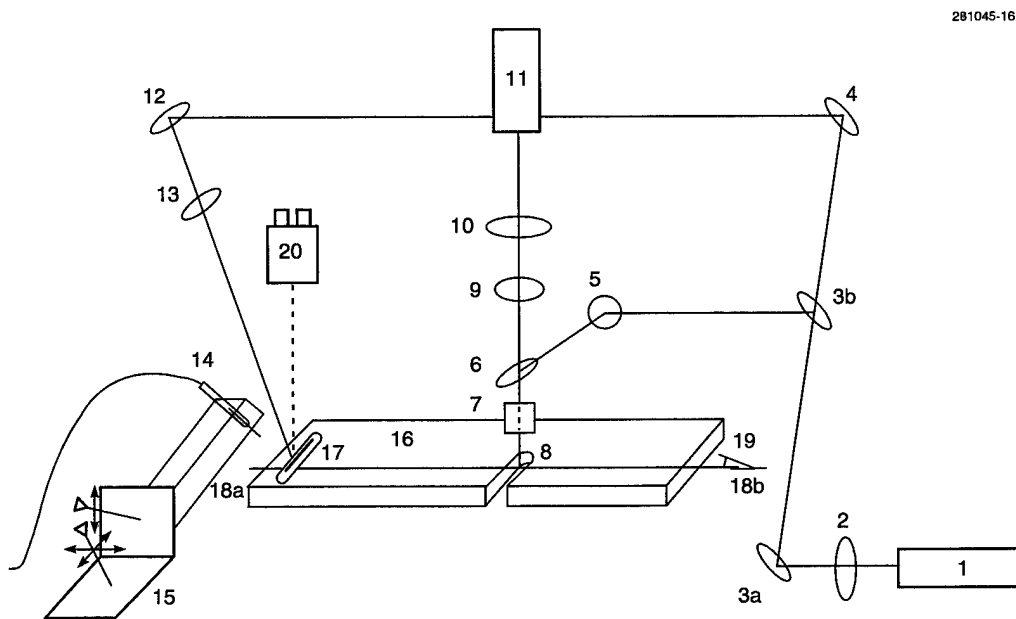


Figure 4-2. Experimental setup using piezoelectric-electrophoretic (PE-EP) injection coupled to epifluorescent laser detection and gel-filled capillaries.

To test the detectability of samples at conventional concentrations, but at greatly reduced volumes, a number of single-droplet experiments have been performed. Figure 4-3 illustrates the results of one such single-droplet injection. This figure shows a train of five single-droplet injection pulses (800 fmol/ μ L FAM-labeled 18-mer oligodeoxynucleotides) spaced at 30-s intervals, followed by three similar pulses spaced at 1-min intervals to reveal the baseline of peak structure. Retention time in this case was 15 min under a 250-V/cm applied field and an L_{eff} of 25 cm. Therefore, we calculate a plug velocity of 280 μ m/s for the oligomer. Hence, the measured full width at half-maximum of 1.5 s leads to a plate count of 1.4×10^6 . These results show the possibility of achieving plate numbers of greater than 10^6 using relatively short separation channels. The components contributing to peak variance can be analyzed using the standard model:

$$\sigma_{\text{Tot}}^2 = \sigma_{\text{inj}}^2 + \sigma_{\text{diff}}^2 + \sigma_{\text{det}}^2 + \sigma_{\text{misc}}^2 ,$$

where the square of the total variance is composed of the sum of the squares of the variances from injection, diffusion, detection, and other sources. We calculate a total plug variance of 210 μ m, which puts an upper limit on the injection variance and hence the size of the injected plug. In fact, from expected diffusion coefficients for 18-mers, we actually expect the majority of the variance to arise from the

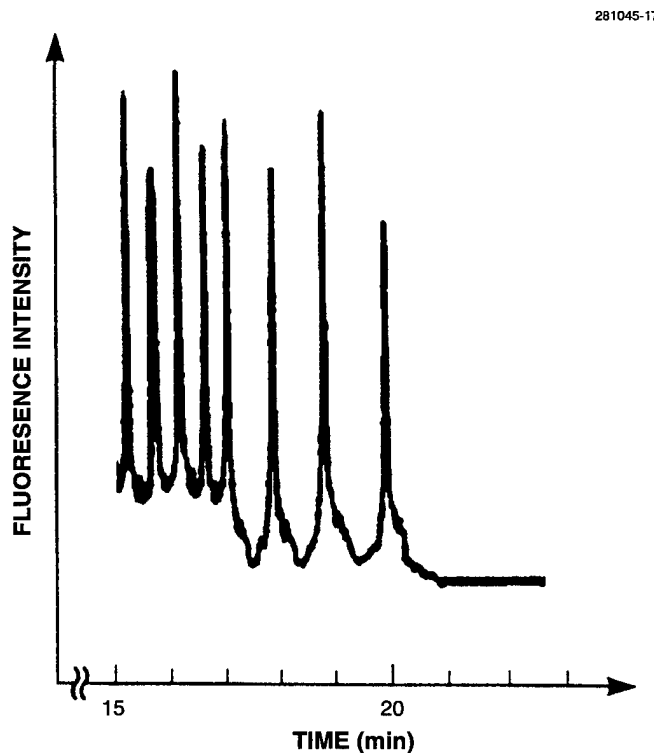


Figure 4-3. Single-droplet PE-EP injection reproducibility and control. Conditions are 800 fmol/ μ L FAM-labeled 18-mer oligonucleotides, $E = 250$ V/cm, $L_{\text{eff}} = 25$ cm.

diffusion component. Thus, by reducing separation distance and time, one may expect to reduce the total variance as well, and thereby further speed analysis while still maintaining adequate resolution. At sample concentrations of 800 fmol/ μ L, the plot shows a signal-to-noise ratio in excess of 100. Therefore, we believe this methodology will be suitable for standard DNA sequencing applications. However, at present the results still show baseline leakage, which reduces the effective signal-to-noise ratio to around 10. This will reduce the effective dynamic range for separations of complex mixtures with closely spaced mobilities.

One advantage of our technique is the flexibility of accurate volumetric injection control by controlling the number of droplets that are used to define the sample plug. In one experiment, a series of sample plugs (100 pmol/ μ L FAM-labeled 18-mer oligodeoxynucleotides) were injected into the capillary at 2-min intervals. These plugs corresponded to nominal volumes of 400, 300, 200, and 100 pL, which in turn correspond to 4, 3, 2, and 1 drops of injected sample. Each peak exhibited a retention time of ~ 72 min under electrophoresis at 72.5 V/cm ($L_{\text{eff}} = 25$ cm). In each of four separate cases, the same injection sequence was used with the largest volume of sample injected first followed by monotonically decreasing volumes of sample. We observe nonlinear injection behavior; Guttman and Schwartz [4] have observed similar effects in consecutive electrokinetic injections from small-volume aqueous samples. Their reported exponential decrease in consecutive peak areas fits our observations well and is attributed to OH^- generation at the cathode. Since these hydroxyl ions are of high mobility, they rapidly build up to the point where they effectively compete with DNA molecules for the ability to carry current within the electrochemical cell. In addition, ionic injection of tris and hydroxyl ions into the buffer reservoir serves to lower resistivity and hence injection efficiency. One can take this electrochemical effect into account by performing exponential curve fits to the data; our average R value for such curve fits is 0.992. There is some variability from run to run, but these measurements demonstrate that volumetric control to within $\pm 15\%$ of a single reference curve is already possible for multidrop injections. Although the quantization of the sample injection is nonlinear because of the electrochemical effect, the consistency of the results demonstrates that reproducibility can be achieved. To date, we have thus demonstrated a quantized injection method which is nonlinear, but which may be extended to the linear regime using conventional injection enhancement strategies.

A. Young
D. Ehrlich*

*Author not at Lincoln Laboratory.

REFERENCES

1. S. I. Zoltan, U.S. Patent No. 3,683,212 (1972).
2. A. Schober, R. Gunther, A. Schwienhorst, M. Doring, and B.F. Lindemann, *BioTechniques* **15**, 324 (1993).
3. L. Wallman, J. Drott, J. Nilsson, and T. Laurell, *8th International Conference on Solid-State Sensors and Actuators and Eurosensors IX: Digest of Technical Papers* (Foundation for Sensor and Actuator Technology, Stockholm, 1995), Vol. 2, p. 303.
4. A. Guttman and H. E. Schwartz, *Anal. Chem.* **67**, 2279 (1995).

5. MICROELECTRONICS

5.1 DOPING PROFILES OF BACK-ILLUMINATED CCDs

Earlier [1],[2], we reported on improvements made to the performance of back-illuminated charge-coupled devices (CCDs), where the thinned CCD had the back surface passivated and ion implanted and the device was annealed in a conventional furnace. We now report on analyses of these devices compared with those fabricated using an earlier technique [3], where the thinned wafer was implanted and then subjected to laser pulse annealing. It can be inferred that the laser-annealed sample has an internal quantum efficiency in the near UV of typically 35 to 45%, while for the furnace-annealed sample the internal quantum efficiency is 90 to 100% [1].

Figure 5-1 is a plot of the doping concentration of the back side of wafers, which is derived from spreading resistance measurements from samples typical of the two processes we have used; the differences in concentration shed light on the differences in performance. It is necessary to have a p^+ concentration gradient on the back surface of the device to drive photoelectrons into the material towards the CCD structure and away from the back surface. For both devices in this plot we have a strong concentration gradient, but the concentration profile exhibited by the furnace-annealed sample is superior for at least two reasons. First, the peak concentration ($\sim 2 \times 10^{18}/\text{cm}^3$ for active boron atoms) is high enough to generate a strong electric field at the back surface, but is not so high as to cause excessive Auger recombination of the photoelectrons, as would happen in the laser-annealed sample, with a surface concentration of $\sim 3 \times 10^{19}/\text{cm}^3$ active boron. Second, the high concentration extends into the furnace-annealed sample to a lesser depth than for the laser-annealed sample, allowing photons with shorter absorption distances to be captured in a region with relatively low boron concentration ($< 1 \times 10^{16}/\text{cm}^3$), again reducing the loss of photoelectrons due to recombination. The laser-annealed sample has a higher maximum gradient, but this is of little importance since, by Gauss' law, the electric field depends on the integral of the dopant profile and not on its slope.

As mentioned previously, the presence of the high-quality oxide on the back of the furnace-annealed sample is important in approaching 100% internal quantum efficiency in the UV, and comparison of the laser-annealed sample and uncoated furnace-annealed sample shows that the external quantum efficiencies are almost identical [1]. The uncoated furnace-annealed sample, however, still has a higher internal quantum efficiency since the damage associated with the laser anneal process serves as a partial antireflective coating, indicating that the difference in doping profile does contribute to the superior performance of the back-illuminated CCD both in the UV and also for soft x-rays [2].

J. A. Gregory

A. H. Loomis

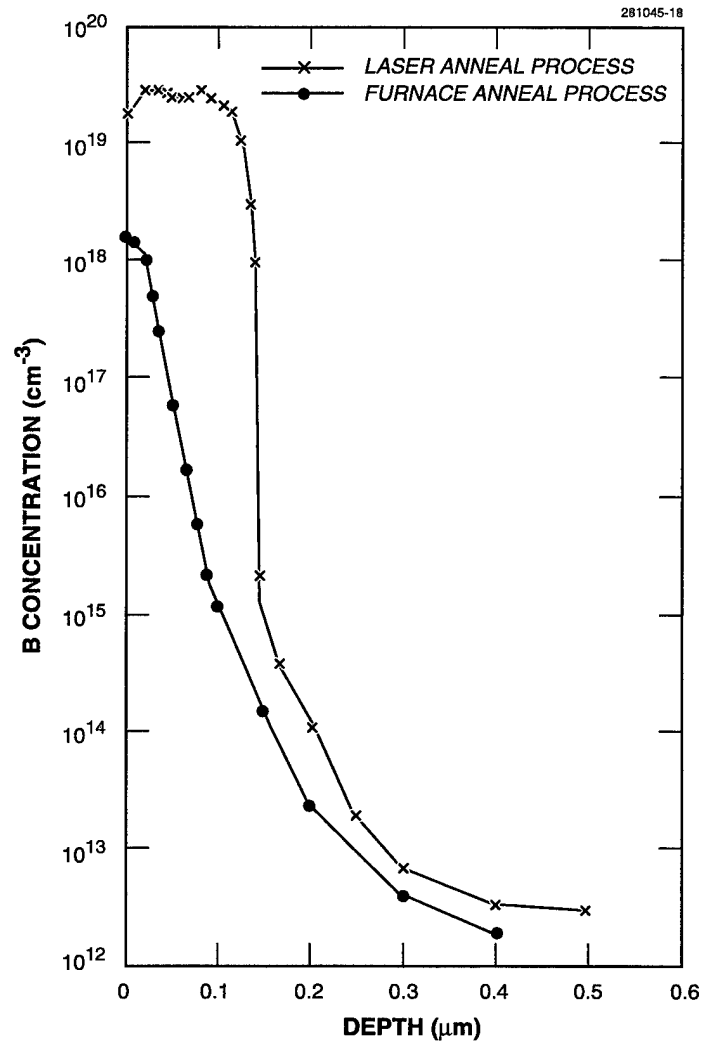


Figure 5-1. Concentration profile of boron dopant on back side of back-illuminated charge-coupled devices.

REFERENCES

1. Solid State Research Report, Lincoln Laboratory, MIT, 1993:1, p. 53.
2. Solid State Research Report, Lincoln Laboratory, MIT, 1994:4, p. 31.
3. C. M. Huang, B. B. Kosicki, J. R. Theriault, J. A. Gregory, B. E. Burke, B. W. Johnson, and E. T. Hurley, *Proc. SPIE* **1447**, 156 (1991).

6. ANALOG DEVICE TECHNOLOGY

6.1 HIGH-POWER YBCO MICROWAVE FILTER

The low surface resistance of the high- T_c superconductor YBaCuO (YBCO) at microwave frequencies holds promise for realizing high- Q filters with sharp bandpass characteristics. Such filters are useful, for example, after a power amplifier to reduce the spurious output generated by amplifier nonlinearities. The surface resistance of YBCO, however, is power dependent [1], and this must be considered in filter design; otherwise the nonlinear behavior of the filter itself will create signals outside the passband. In this report we briefly discuss the synthesis and fabrication of a 0.6% bandwidth, 9-pole Chebyshev transmit filter centered at 2.0 GHz, and present results of CW and pulsed power measurements.

For optimum microwave performance of YBCO, the material must be grown epitaxially as a thin film on a planar substrate, such as lanthanum aluminate (LaAlO_3). This limits the microwave filter topography to planar geometries. We chose to implement a filter using end-coupled microstrip resonators since the intrinsic weak coupling between adjacent resonators is necessary to realize a narrow bandpass response. The filter geometry is shown in Figure 6-1. To preserve filter response linearity at high powers, we minimize current density by using low-impedance resonator sections with wide lines. We used 10- Ω microstrip lines placed along a circle near the edge of a 3-in. substrate. The wider the line, the more power it can handle, but also each filter section deviates more from a rectangular resonator, complicating the filter synthesis.

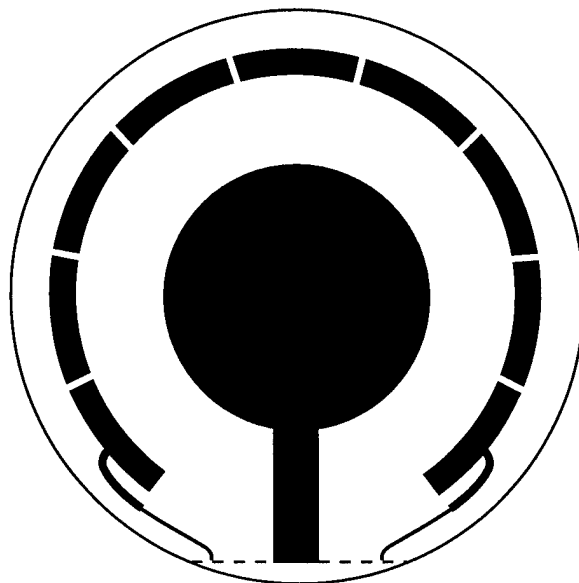


Figure 6-1. Pattern for 9-pole filter. The keyhole-like feature in the center is YBaCuO covered with silver. A similarly shaped spectrum in the package cover makes contact with this pattern using indium washers.

The resonance frequency of each section was calculated using three-dimensional electromagnetic simulators, employing as a start point a rectangular section of the same length calculated with standard microwave formulas. The coupling capacitance between adjacent resonators presented a challenge since the validity of the analytical expressions breaks down for relative dielectric constants higher than 15 (for LaAlO_3 $\epsilon_r = 24$), and the coupling capacitance calculated using different three-dimensional simulators differed by a factor of almost 2. We employed the capacitance values calculated with the three-dimensional simulator that gave the best fit to experiments with weakly coupled resonators, which we use to evaluate film quality.

For Chebyshev filters the input and output coupling is much stronger than the internal coupling between resonators. Since strong capacitive coupling requires very narrow gaps that are difficult to control, we chose instead to use a tap-transformer coupling scheme at the input and output, where the position of the tap with respect to the resonator determines the coupling strength.

Simulation indicates that current crowding occurs where the taps intercept the two end resonators. In past design this current crowding was responsible for failure of 50- Ω , 176- μm -wide input lines, at high input power. To minimize this problem we used a $\lambda/4$ section of a wider line for input and output coupling to a 50- Ω line. This section of line not only could carry more current but its location with respect to the resonator led to less current crowding.

The filter was fabricated on YBCO films deposited by coevaporation on both sides of a 3-in.-diam LaAlO_3 substrate [2]. A 3- μm -thick film of silver was deposited on one side of the substrate and annealed in oxygen for 1 h at 400°C to enhance contact to the YBCO film. A second 2- μm -thick silver film was then deposited over the first silver film. This was necessary since the silver film protects the YBCO during further processing, and the annealing step creates holes in the first silver film. The filter pattern was defined on the uncoated YBCO side, using conventional contact photolithography and a dilute (1/4%) solution of phosphoric acid for etching. Contact regions to the input and output lines were formed using liftoff deposition of an 800-nm-thick silver film.

In the circular geometry we chose, coupling between nonadjacent resonators introduces undesired zeros in the Chebyshev response. Furthermore, the proximity of input and output ports can introduce direct coupling between them which will degrade the out-of-band filter isolation. To minimize these effects we designed a package with a septum in the center that confined the resonators to a waveguide connecting input to output. This waveguide was operated well below cutoff and, consequently, minimized direct coupling and prevented non-nearest-neighbor coupling.

For proper operation of the filter, all resonators must have the same resonance frequency, taking into account the coupling capacitances. However, substrate thickness variations and variations of the local dielectric constant associated with twins in the crystal structure of LaAlO_3 lead to the need for tuning each resonator. Figure 6-2 shows how this was accomplished. Alumina rods were mounted at the end of fine-threaded screws. Bringing the rods closer to the resonators decreases their resonance frequency.

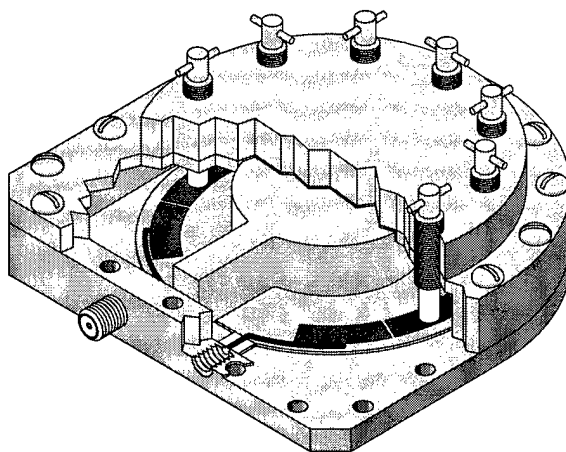


Figure 6-2. Package and tuning mechanism for a 9-pole filter. The package is made of titanium whose expansion coefficient closely matches that of LaAlO_3 .

For testing, the filter package was thermally anchored to the cold finger inside the vacuum enclosure of a cryocooler. A system of mechanical links connected through vacuum feedthroughs allowed the filter to be tuned while cooled to 50 K. Figure 6-3 shows the frequency response for an input power of 7.2 dBm after tuning the filter to minimize ripple. The filter was originally designed for a bandwidth of 0.75% and a ripple of 0.1 dB, but because of the uncertainties in the coupling between adjacent resonators and the position of the input tapping, the best tuning that could be achieved resulted in ripple of close to 2 dB. The measured bandwidth of the filter was 0.6%, indicating lower coupling than desired between resonators. Also shown in Figure 6-3 are the eight frequencies that were used for measurements of the power-handling characteristics of the filter, the results of which are shown in Figure 6-4. Measurements were made at successively higher powers until an excess insertion loss of 0.5 dB was achieved. The filter can handle input power up to 38 dBm for frequencies near the band center and 34 dBm for the out-of-band frequencies where the attenuation is 2 dB. This 4-dB measured difference is expected from calculations of an ideal 0.6% bandwidth, 9-pole Chebyshev filter with 1% ripple although the frequency response that we measured differs from design.

The failure characteristics of various YBCO filters we have measured indicate that a thermal runaway mechanism may be responsible. Usually, the filter response shows little compression up to a certain input power, and fails catastrophically when the input is increased by even a small increment, sometimes < 1 dB. To test this behavior, the power handling of the 9-pole filter was measured with a 500-ns pulsed RF signal at the center of the band. To help understand these measurements we performed a SPICE simulation of the transient response of an ideal 1% ripple, 0.6%-bandwidth, 9-pole Chebyshev filter for a 500-ns RF pulsed 2-GHz signal (center of the band). Each 10- Ω microstrip resonator is modeled by an LCR parallel circuit. The coupling capacitors are calculated using filter synthesis

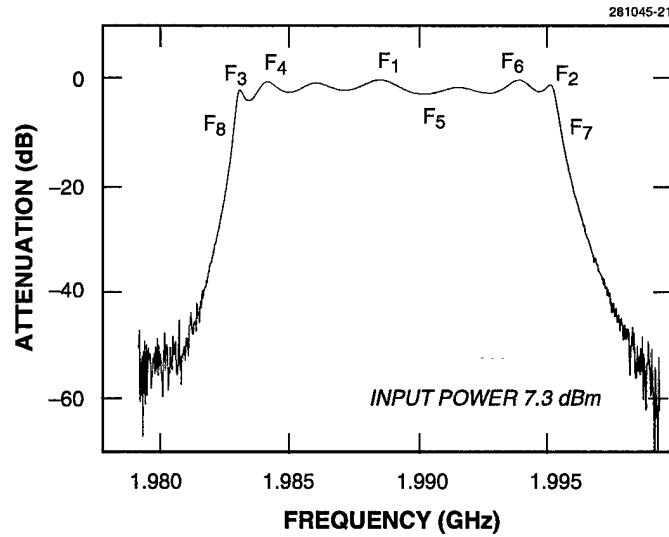


Figure 6-3. Measured frequency response of 9-pole filter for input power of 7.3 dBm. Shown are the frequencies that were used for high-power CW measurements.

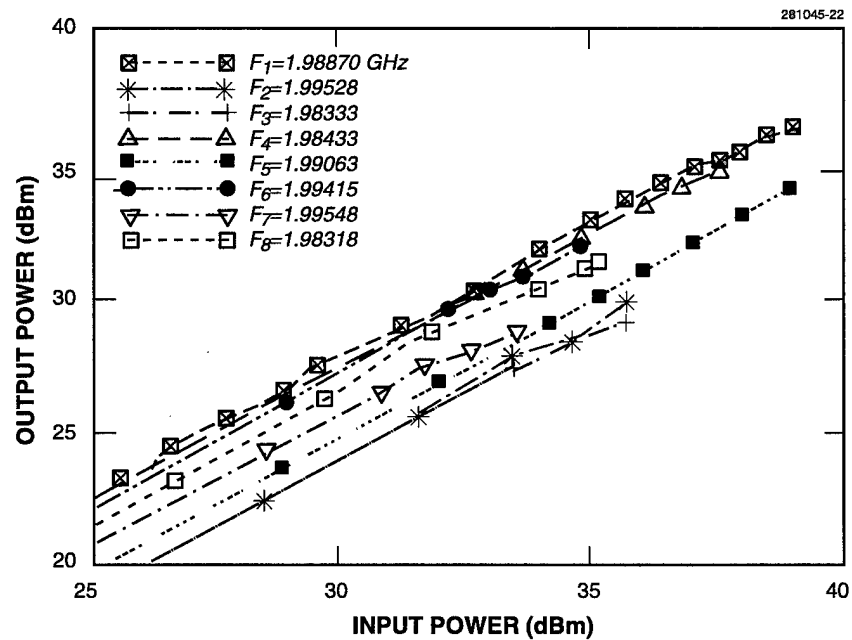


Figure 6-4. Output power as a function of input power for the eight frequencies indicated in Figure 6-3.

techniques [3]. Figure 6-5 shows the expected transient response. The time response shows a number of oscillations, but after 500 ns it has almost reached equilibrium. Figure 6-6 is the measured time response. For input powers up to 40.2 dBm no compression is observed. For an input of 43.3 dBm, less than 1.5 dB of compression is observed. For powers higher than 44.8 dBm the compression is substantial. In fact, for successively higher power, the output power at the center of the pulse drops. It is remarkable, however, that up to powers of 47.6 dBm the filter characteristics do not change irreversibly. This behavior is quite different from what was observed for CW measurements, reinforcing the hypothesis that thermal effects may play a role in the failure mode for these filters.

To bypass the limitations of the simulation tools presently available, we are undertaking a careful experimental evaluation of the input and interresonator coupling coefficients. The method, while tedious, is straightforward. It should be noted that circuit simulations of filters where the elements have been purposely modified to simulate the observed frequency response indicate that a correctly designed Chebyshev filter should allow for higher power-handling capability.

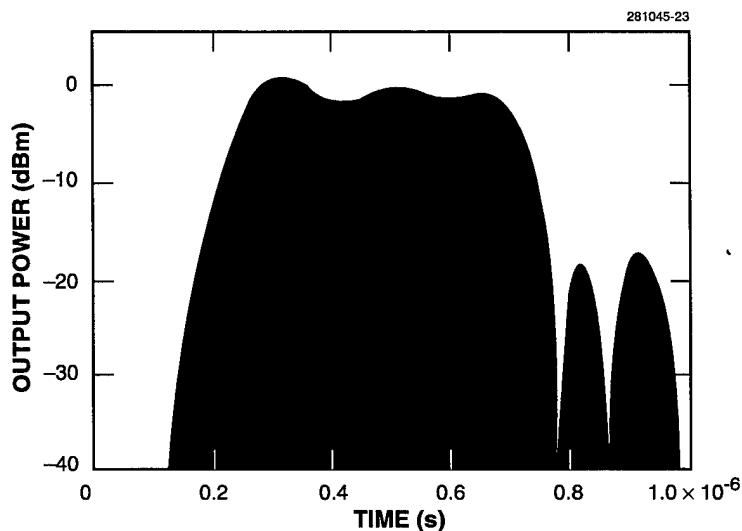


Figure 6-5. Calculated transient response of 9-pole Chebyshev filter having a 0.6% bandwidth and 1% ripple. The pulse length was 500 ns and the center frequency 2.0 GHz.

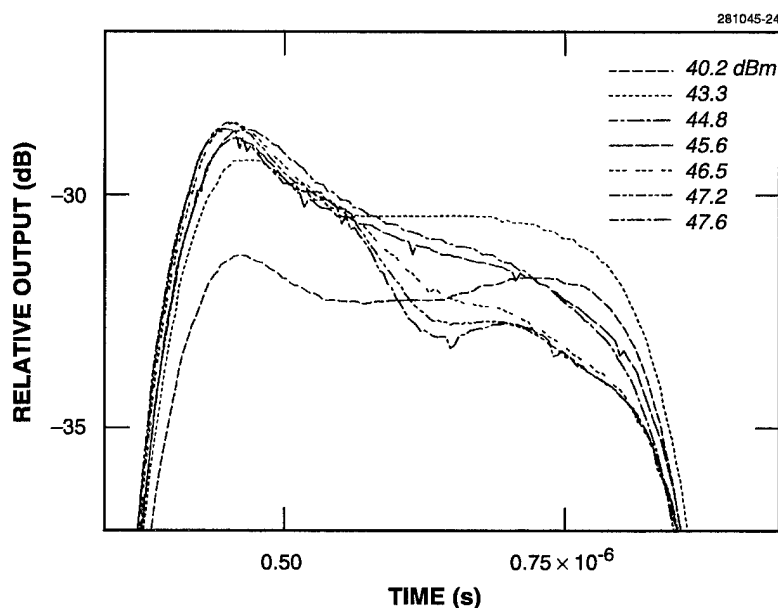


Figure 6-6. Pulsed response for 9-pole filter for different input powers. The RF input pulse was generated by a synthesizer and the transient response measured using a signal analyzer. A number of attenuators were cascaded to prevent saturation of the signal analyzer.

A. C. Anderson	E. de Obaldia*
R. L. Slattery	Z. X. Ma*
P. Polakos*	P. Mankiewich*

REFERENCES

1. P. P. Nguyen, D. E. Oates, G. Dresselhaus, and M. S. Dresselhaus, *Phys. Rev. B* **48**, 6400 (1993).
2. H. Kinder, P. Berberich, B. Utz, and W. Prusseit, *IEEE Trans. Appl. Supercond.* **5**, 1575 (1995).
3. G. L. Matthaei, L. Young, and E. M. T. Jones, *Microwave Filters, Impedance-Matching Networks, and Coupling Structures* (McGraw-Hill, New York, 1964).

*Author not at Lincoln Laboratory.

7. ADVANCED SILICON TECHNOLOGY

7.1 FULLY DEPLETED SOI TECHNOLOGY DEVELOPMENT

A fully depleted silicon-on-insulator (SOI) technology has been developed at Lincoln Laboratory to build integrated circuits designed for very low power operation and fabricated at the limits of optical lithography. A 0.25- μm (drawn gate length) fully depleted SOI CMOS process technology was established using 248-nm optical lithography for initial process demonstrations, and to identify nonlithographic process integration pinch points and SOI material related issues. Design rules and SPICE parameters have been issued for the 0.25- μm technology and a multiproject chip set assembled with circuits submitted by 15 external organizations as well as Lincoln Laboratory. The process technology has been adapted to Lincoln's unique 193-nm step-and-scan tool [1] to fabricate 0.2- μm circuits and provides the world's first application of 193-nm lithography to a complete CMOS process.

The 0.25- μm fully depleted SOI CMOS technology is designed for 0.9-V operation and was developed by utilizing process and device design analytical techniques [2] previously developed for a 0.4- μm bulk CMOS technology. The major features of the technology are thinning of the SOI layer by oxidation to 50 nm; island isolation by silicon etching; sidewall implantation to suppress edge leakage; an 8-nm gate oxide; dual-doped polysilicon gates; a 150-nm spacer oxide; self-aligned TiSi_2 on gates, sources, and drains; and a titanium nitride, aluminum-silicon, and titanium nitride stack deposited at 500°C to fill 0.5- μm contacts. The multilevel metal process includes planarization of a plasma-deposited oxide by chemical-mechanical polishing and deposition of the second metal at 450°C to fill 0.75- μm vias. All layers were defined by plasma etch techniques. The devices reported here were fabricated on SIMOX (separation by implanted oxygen) wafers with buried oxides of 200 and 380 nm.

Ring oscillators and RF amplifiers were constructed with devices that had absolute thresholds < 0.4 V, inverse subthreshold slopes < 70 mV/decade, ΔL of 0.03 and 0.11 μm , and normalized saturated transconductances [3] (transconductance per unit width divided by gate capacitance per unit area) of 0.5 and 0.2×10^7 cm/s for the n - and p -channel devices, respectively. Typical transistor characteristics are shown in Figure 7-1. Ring oscillators and RF amplifiers with gate lengths of 0.25 μm were fabricated with 248-nm lithography. The bandwidth of a 0.25- μm amplifier was 1.62 GHz. The stage delays of 0.2 and 0.25- μm ring oscillators are shown as functions of the power supply voltage in Figure 7-2; both devices had delays < 80 ps at $V_{\text{dd}} = 0.9$ V. For comparison, the ring oscillator speed of the fastest process available from MOSIS, DARPA's silicon foundry, is 120 ps at 3.3 V. The oscillators in Figure 7-2 operate four times faster at the same voltage, and twice as fast with one-tenth the power at 1 V. The 0.2- μm circuit was fabricated using the 193-nm tool for all lithography and is composed of the smallest all-optically defined transistors fabricated to date. The power delay product of the 0.25- μm oscillator with a fanout of three was 0.1 pJ at 1 V as shown in Figure 7-3.

J. A. Burns	H. I. Liu
C. L. Keast	P. W. Wyatt

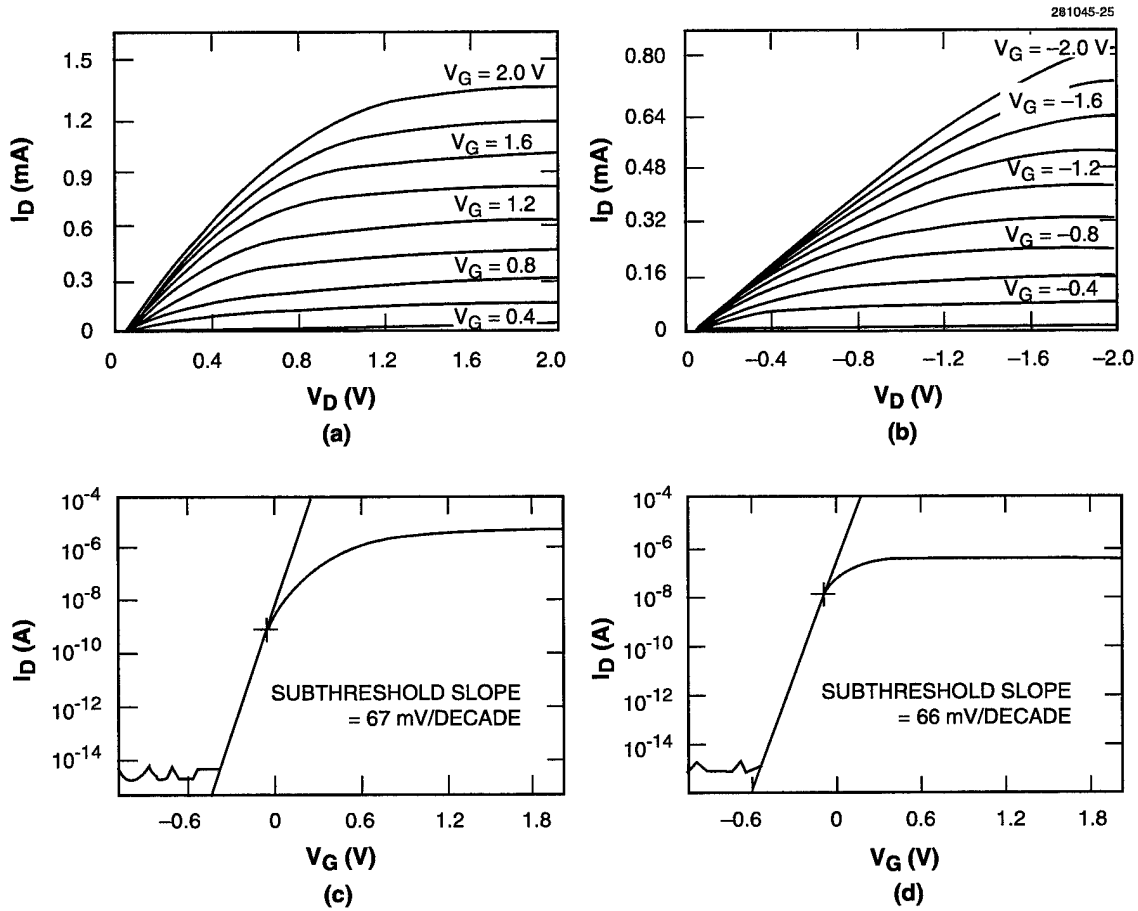


Figure 7-1. Fully depleted transistor results for 50-nm silicon-on-insulator thickness and $W/L = 7/0.25 \mu\text{m}$: (a) n-channel characteristic curves, (b) p-channel characteristic curves, (c) n-channel subthreshold curves, and (d) p-channel subthreshold curves.

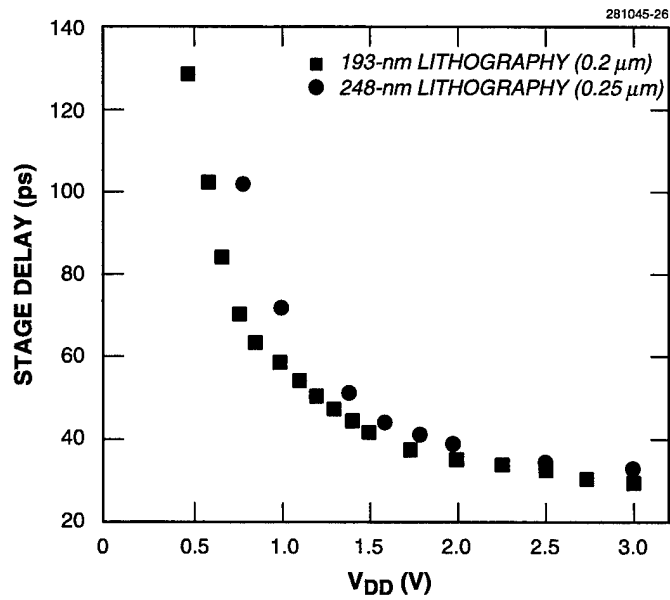


Figure 7-2. Ring oscillator stage delay vs power supply voltage.

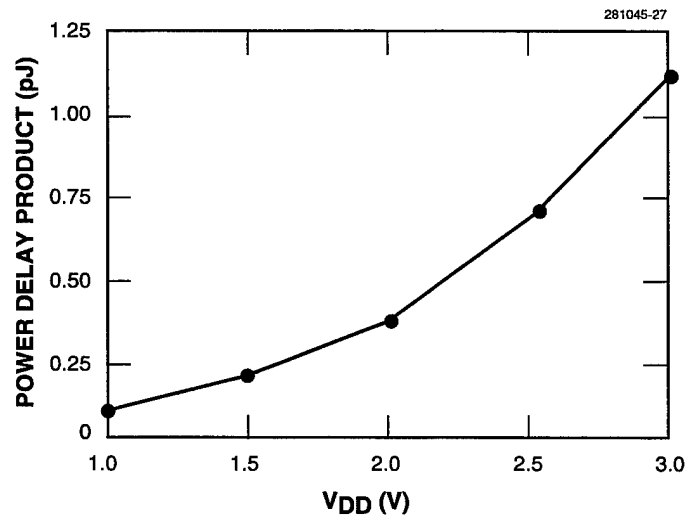


Figure 7-3. Power delay product of 25-stage, 0.25- μ m ring oscillator with fanout of 3.

REFERENCES

1. M. S. Hibbs and R. R. Kunz, *Proc. SPIE* **2440**, 40 (1995).
2. J. A. Burns and G. R. Young, presented at Semiconductor Research Corporation Computer-Integrated Manufacturing IC Workshop, Pittsburgh, Pa., 26 August 1993.
3. D. A. Antoniadis and J. E. Chung, *International Electron Devices Meeting Technical Digest* (IEEE, New York, 1991), p. 21.

